

1 **Dynamical analysis of a reduced model for the North Atlantic Oscillation**

2 Courtney Quinn\*, Dylan Harries, and Terence J. O’Kane

3 *CSIRO Oceans and Atmosphere, Hobart, Tasmania, Australia*

---

4 This manuscript has been submitted for publication in *Journal of the Atmospheric Sciences*.

5 Please note that the manuscript is currently in peer-review. Subsequent versions of this  
6 manuscript may have slightly different content. If accepted, the final version of this manuscript  
7 will be available via the ‘Peer-reviewed Publication DOI’ link. Please feel free to contact the  
8 authors with any feedback.

---

9 \*Corresponding author: Courtney Quinn, courtney.quinn@csiro.au

## ABSTRACT

10 We apply a regularized vector autoregressive clustering technique to identify recurrent and persis-  
11 tent states of atmospheric circulation patterns in the North Atlantic sector ( $110^{\circ}\text{W}$ - $0^{\circ}\text{E}$ ,  $20^{\circ}\text{N}$ - $90^{\circ}\text{N}$ )  
12 associated with the Atlantic Ridge (AR) and the North Atlantic Oscillation (NAO). The technique  
13 additionally provides the temporal behavior in terms of a time-dependent switching between the  
14 respective cluster states. Using the resulting cluster affiliations for each day, we set the switching-  
15 sequence a priori to define a non-smooth linear delayed map that we use to analyze the dynamics  
16 associated with the resulting cluster-based model. We compute the time-dependent covariant Lyapunov  
17 vectors (CLVs) and their associated finite-time covariant Lyapunov exponents (FTCLEs),  
18 with a particular focus on indicators of transitions between the states. We find that the window  
19 chosen to compute the CLVs acts as a filter on the dynamics. For short windows, CLV alignment  
20 and changes in FTCLE growth rates are indicative of individual transitions between persistent  
21 states. For long windows, we observe an emergent annual signal manifest in the alignment of the  
22 CLVs characteristic of the observed seasonality in the respective NAO and AR indices. Analysis  
23 of the average finite-time dimension reveals the  $\text{NAO}^-$  as the most unstable state relative to the  
24  $\text{NAO}^+$ , with persistent AR states largely stable.

## 25 **1. Introduction**

26 The North Atlantic Oscillation (NAO) is a prominent mode of variability in the Northern Hemi-  
27 sphere (NH) atmospheric circulation. Concentrated between the eastern North American and  
28 western European continent, the oscillation characterizes the behavior of large regions of high  
29 and low pressure anomalies over the North Atlantic Ocean. While the background state of at-  
30 mospheric pressure in this region consists of lower pressure to the north and higher pressure in  
31 the mid-latitudes, the NAO describes the modulation to this background state, either enhancing it  
32 (positive phase) or weakening it (negative phase). The changes to the background state of atmo-  
33 spheric pressure over the Atlantic affect wind speed and direction, heat and moisture transport, and  
34 storm numbers and intensity (Hurrell et al. 2013). The instabilities driving transitions between the  
35 phases can develop rapidly and are therefore difficult to predict. This leads to impacts across many  
36 socioeconomic sectors, and therefore motivates further study into the dynamics associated with  
37 such a phenomenon.

38 The two phases of the NAO and their respective associated pressure differences have opposing  
39 effects on the observed atmospheric physics. The positive phase enhances the zonal flow across  
40 the North Atlantic Ocean with much stronger than average westerlies in the mid-latitudes (Visbeck  
41 et al. 2001). These westerlies bring warmer weather to the European continent, particularly in  
42 the winter, as well as stronger and more frequent storms to northern Europe (drier conditions  
43 in southern Europe) (Hurrell 1995). In contrast, the negative phase weakens the mid-latitude  
44 westerlies and is associated with increased blocking events in the North Atlantic region (Shabbar  
45 et al. 2001; Benedict et al. 2004; Croci-Maspoli et al. 2007; Woollings et al. 2008) and anomalously  
46 cold temperatures over the eastern North American and northern European continents (Shabbar  
47 et al. 2001). Although the NAO has variability on interannual and decadal timescales (Hurrell

48 1995; Stephenson et al. 2000), the complicated relationship of the individual NAO phases to  
49 synoptic scale variability makes it a complex phenomenon to study dynamically.

50 An important contributor to the NAO is the interplay between barotropic and baroclinic instability.  
51 Some of the simpler conceptual models proposed for the observed variability of the NAO include  
52 nonlinear barotropic models forced either by a random process imitating baroclinic instability  
53 (Vallis et al. 2004) or a synoptic-scale wave-maker function (Luo et al. 2007a,b,c; Luo and Cha  
54 2012). In the former case, the dipole structure in the pressure field is a result of a dipolar circulation  
55 anomaly caused by the large-scale vorticity stirring in the Atlantic storm track (Vallis et al. 2004).  
56 The latter case emphasizes the importance of a preexisting dipole planetary-scale wave whose  
57 spatial structure must match that of the synoptic-scale wave forcing (Luo et al. 2007a), and it is  
58 shown in such a model that wave-breaking is not a necessary condition for NAO events to occur  
59 (Luo et al. 2007c). When a variable Atlantic mean westerly wind is included in the model, it  
60 can also induce direct transitions between phases (Luo and Cha 2012). There has also been a  
61 considerable amount of work into identifying the dynamical drivers of the NAO through analyzing  
62 the output of general circulation models (GCMs). Feldstein (2003) found that initiation of a  
63 positive phase resulted from anomalous wavetrain propagation, while the negative phase resulted  
64 from in situ growth of the NAO anomaly itself. Other studies have confirmed the necessity of  
65 wave-breaking for the initiation of both phases, with anticyclonic (cyclonic) wave-breaking leading  
66 to a positive (negative) phase (Benedict et al. 2004; Franzke et al. 2004). Franzke et al. (2004) also  
67 conclude that the latitudinal positioning of the Pacific storm track aids in the determination of the  
68 phase. Much work has shown the Madden-Julian oscillation (MJO) is strongly connected to the  
69 phase of the NAO (Frederiksen and Frederiksen 1993; Cassou 2008; Frederiksen and Lin 2013;  
70 Lin et al. 2018). Cassou (2008) found that when the MJO initiates a Rossby wave disturbance in  
71 the western-central tropical Pacific, a positive NAO event was found to occur, whereas negative

72 NAO events resulted from eastern-tropical Pacific or western Atlantic disturbances that modified  
73 the North Atlantic storm track. The MJO-NAO teleconnection can be shown to largely fall within  
74 the general theory for intraseasonal oscillations first proposed by Frederiksen (2002).

75 It is clear from the discussion of the above studies that much remains to be explained regarding the  
76 dynamics governing observed transitions between, and persistence of, the respective NAO phases  
77 and relationship to the associated mid-latitude (Atlantic Ridge, Scandinavian blocking etc), tropical  
78 (MJO), and polar (Arctic Oscillation) teleconnections. One approach that has been suggested to  
79 characterize the instabilities governing changes in atmospheric flow patterns is through the study  
80 of covariant Lyapunov vectors (CLVs). These vectors give a basis on the tangent linear space and  
81 provide directions in phase space of linear perturbations to a nonlinear background flow (Ruelle  
82 1979; Trevisan and Pancotti 1998; Ginelli et al. 2007; Wolfe and Samelson 2007; Kuptsov and  
83 Parlitz 2012). Schubert and Lucarini (2015, 2016) first applied this method to a two-layer quasi-  
84 geostrophic barotropic-baroclinic channel model employing the calculated CLVs to characterize  
85 the stability of, and transitions between, respective zonal and blocked states and to explain the  
86 variance of the modelled atmospheric dynamics. They found that the unstable CLVs showed  
87 enhanced instability during blocked events, where the contributing process to the enhancement  
88 of instability depended on the baroclinicity of the background flow. In a move towards using  
89 more realistic representations of the dynamics, recent studies have employed finite-time dynamical  
90 properties (such as finite-time growth rates of the CLVs or the instantaneous attractor dimension)  
91 to characterize the NAO behavior. The increasing finite-time instability during blocking events  
92 associated with the negative NAO phase was seen in a three-layer quasi-geostrophic model in  
93 spherical geometry (Lucarini and Gritsun 2020), as well as in reanalysis data (Faranda et al. 2017).  
94 This apparent contradiction between the greater than average instability and the expected enhanced  
95 predictability during a persistent blocked flow was suggested to be related to the difficulty in

96 predicting block onset and decay; the formation and decay of a block was found to be associated  
97 with the largest increases in the dimension of the unstable manifold (Lucarini and Gritsun 2020).  
98 Although this increase in finite-time dimension is seen in both theoretical models and the data, it  
99 is not clear whether similar dynamical signals are captured by the widely-used data-driven models  
100 of the observed NAO.

101 In such data-driven models, the NAO must first be extracted by some means from raw observed or  
102 simulated data. Starting from the premise that atmospheric flows exhibit a set of weather regimes  
103 (Legras and Ghil 1985; Vautard 1990; Kimoto and Ghil 1993a), clustering methods (e.g., Mo and  
104 Ghil 1988; Stone 1989; Molteni et al. 1990; Hannachi and Legras 1995; Kidson 2000; Renwick  
105 2005; Straus et al. 2007; Stan and Straus 2007; Fereday et al. 2008; Huth et al. 2008; Pohl and  
106 Fauchereau 2012; Neal et al. 2016) generally detect patterns associated with recurrent behavior or  
107 slow evolution of the system with respect to a reference time-scale. When applied to the circulation  
108 over the North Atlantic (see, e.g., Vautard 1990; Cheng and Wallace 1993; Michelangeli et al. 1995;  
109 Smyth et al. 1999; Cassou et al. 2005; Cassou 2008), a small number of regimes are identified and  
110 may be associated with the NAO as well as preferred blocking patterns. On the other hand, the  
111 simplest clustering-based methods do not explicitly incorporate dynamical information (Harries  
112 and O’Kane 2020), which must be studied using various post hoc approaches (Vautard 1990;  
113 Kimoto and Ghil 1993b; Crommelin 2004; Fereday 2017).

114 Latent variable models, such as hidden Markov models (HMMs) and other state space models  
115 (e.g., Majda et al. 2006; Franzke et al. 2008, 2011), attempt to better account for these important  
116 dynamical aspects. HMM studies of the North Atlantic circulation have been shown to identify  
117 persistent hidden regimes corresponding to the NAO and East Atlantic pattern (Franzke et al. 2011)  
118 and used to study signals relating to regime transitions (Franzke et al. 2011; Tantet et al. 2015).

119 On the other hand, the assumption that the flow is well-described by a time-homogeneous Markov  
120 chain need not be satisfied in practice, nor are the extracted regimes necessarily metastable.

121 One such approach that has recently been found to be effective in extracting metastable regimes  
122 states makes use of the so-called finite element clustering with bounded variation (FEM-BV)  
123 framework (Franzke et al. 2009; Horenko 2009, 2010a,b; Metzner et al. 2012). As in an HMM,  
124 the FEM-BV method presumes the existence of a finite number of hidden states, each having time-  
125 independent properties, and a switching process describing transitions between the states. This  
126 switching process is not required to be governed by a Markov chain; instead, the model is regularized  
127 to enforce some level of persistent residence in the states. The system is thus described in terms  
128 of a set of locally stationary states, e.g., in the FEM-BV-VAR method, by locally stationary linear  
129 vector autoregressive (VAR) processes. In applications to the mid-latitude troposphere (O’Kane  
130 et al. 2013b; Franzke et al. 2015; Risbey et al. 2015; O’Kane et al. 2016, 2017; Falkena et al. 2020)  
131 and large-scale ocean circulation (O’Kane et al. 2013a), the FEM-BV-VAR method and its variants  
132 have been found to identify persistent states that can be identified as large-scale coherent structures.  
133 Additional applications of the FEM-BV-VAR method include studies of the atmospheric boundary  
134 layer (Vercauteren and Klein 2015; Vercauteren et al. 2016).

135 The above studies have demonstrated that the FEM-BV-VAR method extracts reasonable  
136 metastable states. The associated switching sequences, on the other hand, have received less  
137 attention, with most focus given to investigating multiyear trends in the occurrence of states  
138 (O’Kane et al. 2016, and references therein) and their association with extremes (Risbey et al.  
139 2018). At shorter time-scales, it might be hoped that the state transition sequence captures at least  
140 some aspects of the dynamics associated with regime transitions, in spite of the severe dimension  
141 reduction involved in formulating the model. In this study, we investigate this question in the  
142 context of a model for the NAO derived from an FEM-BV-VAR cluster analysis. When applied to

143 the atmospheric circulation in the Atlantic sector, the FEM-BV-VAR method yields a set of states  
144 consistent with differing phases of the NAO. By treating the clustering as a non-smooth linear  
145 delay system, it is possible to directly compute the Lyapunov spectrum and CLVs of the model, as  
146 well as dynamical indicators of transitions such as increased finite-time instability (Norwood et al.  
147 2013) and alignment of CLVs (Beims and Gallas 2016; Sharafi et al. 2017; Kuptsov and Kuznetsov  
148 2018). The relationship between these dynamical quantities and the particular regime transitions  
149 can then be compared to assess whether the reduced-order model exhibits non-trivial dynamics.

150 In this study we analyze the optimal model for the NAO resulting from applying the FEM-BV-  
151 VAR method to atmospheric reanalysis data. The remainder of this article is structured as follows.  
152 In section 2 the data and clustering methods used to derive a reduced order model for circulation  
153 regimes is described. We introduce the general properties of the optimal model and validate it  
154 against an observed NAO index. In section 3 we define the corresponding discrete time dynamical  
155 system through construction of a delay-embedded non-smooth linear map that corresponds to the  
156 time-dependent dynamics of the optimal model from the fit. Through this novel interpretation of  
157 the system we calculate the corresponding CLVs and their properties as they evolve in time. We  
158 focus on the characterization of persistent states and analyze how the dynamical properties relate  
159 to the transitioning behavior of the model, both on short and long time-scales. Finally, in section  
160 4 we summarize our findings.



## 2. Identifying North Atlantic circulation regimes

### *a. Data*

We examine the NH mid-tropospheric circulation in terms of daily mean 500 hPa geopotential height ( $Z_{g500 \text{ hPa}}$ ) fields obtained from the National Centers for Environmental Prediction/National Center for Atmospheric Research (NCEP/NCAR) Reanalysis 1 (Kalnay et al. 1996).

The NCEP/NCAR Reanalysis 1 (NNR1) atmospheric reanalysis spans 1948 to present with a T62 resolution on 28 vertical levels and is constrained by both surface and atmospheric observational data. The  $Z_{g500 \text{ hPa}}$  data are provided on a global  $2.5^\circ \times 2.5^\circ$  latitude-longitude grid, from which we compute daily height anomalies,  $Z'_{g500 \text{ hPa}}$ , by subtracting the daily climatological mean determined from the 1 January 1979 to 31 December 2018 reference period. An initial dimension reduction is carried out by performing an EOF analysis of the latitude-weighted daily height anomalies in the North Atlantic sector ( $110^\circ\text{W} - 0^\circ\text{E}$ ,  $20^\circ\text{N} - 90^\circ\text{N}$ ) between 1 January 1979 and 31 December 2018, including all seasons. This preprocessing step is required to reduce the overall dimensionality of the data in order to render the subsequent clustering analysis, now applied to the retained principal components (PCs) rather than the full gridded fields, tractable. Otherwise, no further use is made of the corresponding spatial patterns in defining the extracted regimes. The number of PCs retained should be large enough to capture the relevant dynamics driving the processes of interest, while at the same time not being so large that the clustering problem is ill-posed. In carrying out sensitivity analyses with respect to the number of retained PCs, it was found that  $d = 10$  PCs was insufficient to capture the meridionally oriented dipolar structures associated with the NAO, with the reduced order model states instead tending to consist of predominantly zonally oriented wavetrains, as previously observed in O’Kane et al. (2017). For  $d = 20$  PCs, on the other hand, we find that the expected structures are found in the reduced order model, as discussed below. In the following we

184 therefore choose to keep the leading  $d = 20$  PCs, accounting for approximately 91% of the total  
 185 variance; the corresponding EOFs are shown in appendix A. Additionally, to assess the qualitative  
 186 behavior of the regimes identified by the clustering analysis, we make use of the daily NAO index<sup>1</sup>  
 187 provided by the National Oceanic and Atmospheric Administration Climate Prediction Center  
 188 (NOAA CPC), computed from a rotated EOF analysis of standardized 500 hPa geopotential height  
 189 anomalies (Barnston and Livezey 1987).

190 *b. FEM-BV-VAR clustering*

191 Given the daily timeseries of  $d = 20$  PCs between 1 January 1979 and 31 December 2018,  
 192 corresponding to a sample of length  $T = 14610$  days, we next extract a set of persistent states by  
 193 applying the FEM-BV-VAR clustering method (Horenko 2010b; Metzner et al. 2012).

194 In this approach, the behavior of the system is taken to be described by an underlying model  
 195 determined by a set of generally time-dependent parameters  $\Theta(t)$ . Specifically, in the FEM-BV-  
 196 VAR case, the stochastic model is taken to be of the form

$$\mathbf{x}_t = \boldsymbol{\mu}(t) + \sum_{\tau=1}^m \mathbf{A}_\tau(t) \mathbf{x}_{t-\tau} + \boldsymbol{\epsilon}_t \quad (1)$$

197 where  $\Theta(t) = (\boldsymbol{\mu}_t, \mathbf{A}_1(t), \dots, \mathbf{A}_m(t), \boldsymbol{\Sigma}(t))$  is a vector of time-dependent model parameters for an  
 198 order  $m$  linear autoregressive model with mean vector  $\boldsymbol{\mu}(t)$  and random noise  $\boldsymbol{\epsilon}_t$  with time-varying  
 199 covariance matrix  $\boldsymbol{\Sigma}(t)$ . To arrive at a well-posed problem for estimating the model parameters,  
 200 it is then assumed that the full, non-stationary system can be well approximated in terms of  
 201 transitions between a finite set of  $K$  states. These states are assumed to be individually stationary  
 202 and determined by a set of fixed, time-independent parameters  $\Theta_i$ ,  $i = 1, \dots, K$ , i.e., the system is  
 203 assumed to be locally stationary (Metzner et al. 2012). The original time-dependence of the model  
 204 parameters then arises via the switching of the system between states. The time-scales associated

---

<sup>1</sup><https://www.cpc.ncep.noaa.gov/products/precip/CWlink/pna/nao.shtml>

205 with the individual states and with the underlying switching process may in general differ, making  
 206 the method suitable for analyzing the multiscale dynamics typical of the atmospheric circulation.  
 207 The resulting model is interpreted as representing the observed fields in terms of a set of recurrent  
 208 circulation regimes that govern the local, short-term (e.g., day-to-day) variability, which the system  
 209 repeatedly transitions between.

210 To determine both an assignment of individual days to a state as well as the parameters  $\Theta_i$   
 211 characterizing each state, we minimize a loss function of the form

$$L(\Theta, \Gamma) = \frac{1}{T} \sum_{t=1}^T \sum_{i=1}^K [\gamma_t]_i \ell_i(\mathbf{x}_t, \Theta_i), \quad (2)$$

212 where  $\mathbf{x}_t \in \mathbb{R}^d$  denotes the vector of PCs at time  $t$ ,  $\Theta = (\Theta_1, \dots, \Theta_K)$  denotes the combined set of  
 213 parameters for all states, and the functions  $\ell_i(\mathbf{x}_t, \Theta_i)$  are appropriately chosen loss functions for  
 214 each of the  $K$  states quantifying the level of fit under that state for given  $\Theta_i$ , e.g., the squared error  
 215 or negative log-likelihood. The sequence of state assignments is encoded by the state affiliations  
 216  $\gamma_t \in \mathbb{R}^K$ . At a given time  $t$ , these affiliations are required to satisfy

$$\sum_{i=1}^K [\gamma_t]_i = 1, \quad [\gamma_t]_i \geq 0 \quad \forall i = 1, \dots, K, \quad (3)$$

217 such that the loss function is a convex combination of the individual losses and the complete set  
 218 of affiliations  $\Gamma^T = [\gamma_1^T, \dots, \gamma_T^T] \in \mathbb{R}^{K \times T}$  may be interpreted as providing a soft clustering of the  
 219 data into the  $K$  states. The observed persistence of large-scale coherent features in the mid-latitude  
 220 troposphere implies that the switching process described by the affiliations  $\Gamma$  should also exhibit  
 221 some degree of persistence, yielding regimes that are metastable. To enforce this behavior, the  
 222 affiliation sequence is required to satisfy a constraint on the total variation norm of the sequence<sup>2</sup>,

---

<sup>2</sup>In the usual formulation of FEM-BV clustering, it is further assumed that the affiliations can be expressed in terms of a set of compactly supported basis functions. When each basis function is non-zero over more than one time step, this essentially imposes a minimum length of time that must be spent in a given state. We choose triangular basis functions that are non-vanishing at only a single time point, allowing state transitions between adjacent time points.

223 of the form

$$\sum_{t=1}^{T-1} |[\gamma_{t+1}]_i - [\gamma_t]_i| \leq C_T, \quad \forall i = 1, \dots, K, \quad (4)$$

224 for some constant  $C_T$ . Each term in this sum is non-zero only if the affiliations differ between  
 225 times  $t$  and  $t + 1$ , corresponding to a transition between states, so that this constraint imposes an  
 226 upper bound on the total number of transitions between states. It is more convenient to express this  
 227 constraint in terms of a "typical" state length  $p \geq 0$  that is independent of the time series length, in  
 228 terms of which we define  $C_T$  as

$$C_T = \frac{T}{p} - 1. \quad (5)$$

229 The form of the loss functions  $\ell_i(\mathbf{x}_t, \Theta_i)$  is governed by the assumed dynamics within the hidden  
 230 states. For the FEM-BV-VAR clustering method, the time evolution of the system within a given  
 231 state is described by Eq. (1) where  $\Theta(t)$  is replaced by  $\Theta_i = (\boldsymbol{\mu}^{(i)}, \mathbf{A}_1^{(i)}, \dots, \mathbf{A}_m^{(i)}, \boldsymbol{\Sigma}^{(i)})$  for each state  
 232  $i \in \{1, \dots, K\}$ . For simplicity, we assume the same order  $m$  for all  $K$  states; moreover, we assume  
 233 that some number  $m_{\max} \geq m$  of samples are held-out from the start of the time series to provide  
 234 the required initial values, leaving  $T - m_{\max}$  samples to be modeled. A particular state is then fully  
 235 specified by the parameters  $\Theta_i$ , and the corresponding loss function is chosen to be the squared  
 236 residual

$$\ell_i(\mathbf{x}_t, \Theta_i) = \left\| \mathbf{x}_t - \boldsymbol{\mu}^{(i)} - \sum_{\tau=1}^m \mathbf{A}_\tau^{(i)} \mathbf{x}_{t-\tau} \right\|^2. \quad (6)$$

237 A numerical method for finding the minimum of the resulting loss function with respect to  $\Theta$  and  
 238  $\Gamma$  is summarized in appendix B.

239 The number of clusters  $K$ , VAR order  $m$ , and state length  $p$  constitute the set of hyperparameters  
 240 that must be chosen beforehand when applying the above procedure. To determine reasonable  
 241 choices for these hyperparameters, we perform a grid search over all combinations of  $K \in \{1, 2, 3\}$ ,  
 242  $m \in \{0, 1, 2, 3, 4, 5\}$  days (requiring  $m_{\max} = 5$  days), and  $p \in \{0, 5, 10, \dots, 55, 60\}$  days. To compare

243 models with different hyperparameter settings, we use a rolling origin cross-validation procedure  
 244 (described in appendix B) to generate estimates of the out-of-sample reconstruction root mean  
 245 square error (RMSE) for each combination of hyperparameters. Lower values for this measure  
 246 indicate a reasonable compromise between fitting the data well without overfitting to the training  
 247 data, and so we select as our optimal model the set of hyperparameters that minimize this metric.  
 248 The results of this cross-validation procedure, using  $N_{\text{fold}} = 10$  cross-validation folds, are summa-  
 249 rized in FIG. 1. The minimal mean test set reconstruction RMSE is found for  $K = 3$  states,  $m = 3$   
 250 days, and a typical state length of  $p = 5$  days. The reconstruction error is, however, rather similar  
 251 for  $K = 2$  or  $3$ ,  $m \geq 3$  days, and  $p \leq 20$  days, indicating relatively low sensitivity to the choice of  
 252 persistence so long as the state length is sufficiently short. We note that a typical state length of  
 253  $\sim 5$  days is consistent with previous results identifying Euro-Atlantic regimes with an FEM-BV  
 254 variant of  $k$ -means clustering (Falkena et al. 2020) in which an optimal value of 6.8 days is found  
 255 based on information criteria applied with a fixed number of  $K = 4$  clusters.

### 256 *c. Properties of the optimal model*

257 Given the fitted affiliation sequence corresponding to the selected model, we assign each time to  
 258 a state  $i_t \in \{1, 2, 3\}$  according to

$$i_t = \arg \max_j [\gamma_t]_j. \quad (7)$$

259 We do not place a threshold on the number of consecutive days used to define a state, as some  
 260 level of persistence is already built-in to the clustering model. Composites of the height anomalies  
 261 assigned to each state in this way are shown in FIG. 2 for the optimal model with  $K = 3$  states,  
 262 memory  $m = 3$  days, and typical state length  $p = 5$  days. Two states strongly resemble the positive  
 263 and negative phases of the NAO (Barnston and Livezey 1987), denoted in FIG. 2 by  $\text{NAO}^+$  and  
 264  $\text{NAO}^-$ , respectively. The remaining state is somewhat similar to the East Atlantic pattern or

265 Atlantic Ridge (AR) pattern (Straus et al. 2017), representing blocking activity in the mid-Atlantic  
266 and which has previously been linked to surface temperature extremes in western Europe (Plaut and  
267 Simmonet 2001; Cassou et al. 2005). TABLE 1 and TABLE 2 summarize the temporal characteristics  
268 of the states in terms of the number of consecutive days spent resident within each state and the  
269 frequency of particular transitions. The model has much longer maximum residency lengths in the  
270 NAO<sup>-</sup> state than in the NAO<sup>+</sup> or the AR states, and generally remains in the NAO<sup>-</sup> state for longer  
271 than either of the other two states. For all three states, the minimum length of time spent in the  
272 state is one day, indicating the presence of periods of rapid switching between states. In particular,  
273 this implies that fast dynamics, with a time-scale of a day or so, are present in the model in addition  
274 to the persistent states. The number of consecutive days spent within a state exhibits a seasonal  
275 cycle, with long runs of NAO<sup>-</sup> states occurring during the boreal summer (JJA) and more equal  
276 state lengths during DJF. This is also evident in TABLE 2, which shows a predominance of NAO<sup>-</sup>  
277 states during JJA and fewer state transitions overall. The NAO<sup>-</sup> state occurs least frequently during  
278 DJF, when most days are assigned to the AR and NAO<sup>+</sup> states; the former state is associated in all  
279 seasons with a weakening of the mid-latitude zonal flow and in particular with lower maxima in  
280 the zonal mean low-level westerlies over the Atlantic, which are more typical of the JJA flow (not  
281 shown). Transitioning between states occurs more frequently outside of boreal summer. At the  
282 level of particular state transitions, the number of transitions out of the NAO<sup>-</sup> state is essentially  
283 unchanged between DJF and JJA. In JJA, transitions occur preferentially to and from the NAO<sup>-</sup>  
284 state, while in DJF a larger proportion of transitions are between the AR and NAO<sup>+</sup> states.

285 The state assignments produced by the FEM-BV-VAR fit provide a discrete index measuring the  
286 expression of the associated mode on each day. To verify that the occurrence of the NAO-like  
287 states shown in FIG. 2 reflects the observed behavior of the NAO, we compare the model affiliation  
288 sequence to the NOAA CPC NAO index. As a measure of similarity, we compare the percentage

289 of days assigned to the  $\text{NAO}^-$  state with the percentage of days that the CPC index is negative,  
 290 defining an  $\text{NAO}^-$  residency percent for both the model and the continuous index. To focus on  
 291 longer term variability, we compare either the result of computing the residency percent over a one  
 292 year sliding window, i.e.,

$$\begin{aligned}
 R_{SW}^{\text{model}}(t) &= \sum_{t'=t-365}^t \frac{\mathbb{I}(i_{t'} = 2)}{365}, \\
 R_{SW}^{\text{CPC}}(t) &= \sum_{t'=t-365}^t \frac{\mathbb{I}(\text{CPC index}(t') < 0)}{365},
 \end{aligned} \tag{8}$$

293 where  $\mathbb{I}(x)$  is an indicator function equal to one if  $x$  is true and zero otherwise, or by applying  
 294 a LOWESS smoothing (Cleveland 1979) to the fraction of  $\text{NAO}^-$  days in each year. The results  
 295 of this comparison are shown in FIG. 3. There is a high correlation between the percent of days  
 296 assigned to the  $\text{NAO}^-$  state in the model and the percent of days with a negative NAO index  
 297 ( $r \approx 0.74$  between the sliding window time series and  $r \approx 0.8$  for the series of annual counts),  
 298 suggesting that occurrences of the FEM-BV-VAR  $\text{NAO}^-$  state do broadly correspond to conditions  
 299 characteristic of the negative phase of the NAO. Comparable results were found by Risbey et al.  
 300 (2015).

### 301 3. Dynamical Analysis

302 Based on the above analysis we have some confidence that the optimal FEM-BV-VAR model  
 303 extracts a set of metastable states that can be related to coherent features in the North Atlantic.  
 304 We next assess whether a simplified dynamical model derived from this fit can be used to study  
 305 the dynamics associated with regime transitions between those states. To do so, the optimal FEM-  
 306 BV-VAR fit with  $K = 3$ ,  $m = 3$  days, and  $p = 5$  days can be naturally interpreted as a discrete time

307 system based on Eq. (1) in which the time evolution is given by

$$\mathbf{x}_{t+1} = \begin{cases} \boldsymbol{\mu}^{(1)} + \mathbf{A}_1^{(1)} \mathbf{x}_t + \mathbf{A}_2^{(1)} \mathbf{x}_{t-1} + \mathbf{A}_3^{(1)} \mathbf{x}_{t-2}, & \text{for } i_{t+1} = 1, \\ \boldsymbol{\mu}^{(2)} + \mathbf{A}_1^{(2)} \mathbf{x}_t + \mathbf{A}_2^{(2)} \mathbf{x}_{t-1} + \mathbf{A}_3^{(2)} \mathbf{x}_{t-2}, & \text{for } i_{t+1} = 2, \\ \boldsymbol{\mu}^{(3)} + \mathbf{A}_1^{(3)} \mathbf{x}_t + \mathbf{A}_2^{(3)} \mathbf{x}_{t-1} + \mathbf{A}_3^{(3)} \mathbf{x}_{t-2}, & \text{for } i_{t+1} = 3, \end{cases} \quad (9)$$

308 where  $i_t$  is the fitted state assignment given by Eq. (7). The cluster means  $\boldsymbol{\mu}^{(1)}, \boldsymbol{\mu}^{(2)}, \boldsymbol{\mu}^{(3)}$  and  
 309 parameter matrices  $\mathbf{A}_i^{(k)}$  for  $i, k \in \{1, 2, 3\}$  are constant. Note that, by constructing the model in  
 310 such a way, the dynamics will change in the time step prior to a transition in the affiliation sequence.

311 We are interested in whether the dynamical properties of the resulting model from the FEM-  
 312 BV-VAR framework can show any insight on the mechanisms characterizing transitions between  
 313 states and whether the reduced dynamical model exhibits properties that are physically plausible.  
 314 In order to study the dynamics we use the resulting affiliation sequences and parameter matrices  
 315 from the optimal FEM-BV-VAR model to construct the following system:

$$\begin{bmatrix} \mathbf{x}_{t+1} \\ \mathbf{x}_t \\ \mathbf{x}_{t-1} \end{bmatrix} = \begin{bmatrix} \mathbf{A}_1^{(i_{t+1})} & \mathbf{A}_2^{(i_{t+1})} & \mathbf{A}_3^{(i_{t+1})} \\ \mathbf{I} & \mathbf{0} & \mathbf{0} \\ \mathbf{0} & \mathbf{I} & \mathbf{0} \end{bmatrix} \begin{bmatrix} \mathbf{x}_t \\ \mathbf{x}_{t-1} \\ \mathbf{x}_{t-2} \end{bmatrix}. \quad (10)$$

316 Eq. (10) describes a discrete non-smooth linear mapping system governing the tangent dynamics  
 317 of Eq. (9), with a finite number of transitions between states defined a priori by the switching  
 318 sequence Eq. (7). As we retain the leading  $d = 20$  PCs, the system Eq. (10) has a 60-dimensional  
 319 state space. The matrices  $\mathbf{I}$  are 20-dimensional identity matrices, and  $\mathbf{0}$  denotes the  $20 \times 20$  zero  
 320 matrix.

321 We can now analyze dynamical properties of this system. The linear map defined by Eq. (10)  
 322 combined with the switching sequence, Eq. (7), defines the matrix cocycle, or the forward and  
 323 backward mapping of solutions under the tangent dynamics. In other words, let the cocycle  $\mathcal{A}(t, \tau)$



324 be defined as

$$\mathcal{A}(t, \tau) = \mathcal{A}(t + \tau, 0) \dots \mathcal{A}(t, 0), \quad (11)$$

325 where  $\mathcal{A}(t, 0)$  is the linear propagator defined by

$$\mathcal{A}(t, 0) = \begin{bmatrix} \mathbf{A}_1^{(i_{t+1})} & \mathbf{A}_2^{(i_{t+1})} & \mathbf{A}_3^{(i_{t+1})} \\ \mathbf{I} & \mathbf{0} & \mathbf{0} \\ \mathbf{0} & \mathbf{I} & \mathbf{0} \end{bmatrix}. \quad (12)$$

326 We use the cocycle  $\mathcal{A}(t, \tau)$  to calculate the CLVs of the system in Eq. (10). The CLVs  $\phi_i$  satisfy  
 327 the Multiplicative Ergodic Theorem (Oseledets 1968),

$$\lambda_i = \lim_{\tau \rightarrow \infty} \frac{1}{\tau} \log \|\mathcal{A}(t, \tau) \phi\| \quad \text{iff} \quad \phi \in \Phi_i(t) \setminus \Phi_{i+1}(t) \quad (13)$$

328 where  $\lambda_i$  is the asymptotic growth rate of vectors in subspace  $\Phi_i$ . Although the linear maps are not  
 329 explicitly time dependent, the cocycle is implicitly time-dependent through the switching sequence,  
 330 Eq. (7). We calculate the CLVs using algorithm 2.2 from Froyland et al. (2013), which is also  
 331 summarized in Quinn et al. (2020). The CLV calculation contains two parameters that one must  
 332 make a choice for: the push forward step  $M$  and the reorthogonalization step  $n$ . Due to the short  
 333 residency in a given state, we use a reorthogonalization step of  $n = 1$  day. It is not immediately  
 334 clear what push forward step to use, so we compute the CLVs for the following range of push  
 335 forward steps:  $M = 3, 10, 30, 50$  days.

336 In the following sections we investigate the growth rates and alignment of the leading CLVs.  
 337 We compare the behavior for the different push forward steps and analyze how changes in either  
 338 property relates to transitions between the states.

339 *a. Finite-time covariant Lyapunov exponents*

340 The first property of the CLVs that we analyze is their finite-time growth rates, i.e., finite-  
 341 time covariant Lyapunov exponents (FTCLEs). Due to the rapid transitioning between states,  
 342 we consider the growth rates over the course of one day. We define the FTCLEs as in Wolfe  
 343 and Samelson (2007), here Eq. (14a). To calculate the FTCLEs we use a forward difference  
 344 approximation to the derivative, which in our case simplifies to applying the linear propagator to  
 345 the CLV calculated for a given day and taking the difference of the  $L^2$ -norms:

$$\Lambda_i(t) = \frac{1}{\|\phi_i(t)\|} \frac{d}{dt} \|\phi_i(t)\| \quad (14a)$$

$$= \|\mathcal{A}(t,0)\phi_i(t)\| - \|\phi_i(t)\|. \quad (14b)$$

346 Note that  $\|\phi_i(t)\| = 1$  for CLVs computed using the Froyland et al. (2013) algorithm and therefore  
 347 the scaling factor is omitted from Eq. (14b).

348 We compare the FTCLEs computed using Eq. (14b) to the asymptotic growth rates computed  
 349 from the QR decomposition method (appendix C). For the computation we use the full matrix  
 350 cocycle over the period of the FEM-BV-VAR fit and an orthonormalization time step of 1 day.  
 351 We find that asymptotically the model is stable and there is little evidence of a spectral gap in  
 352 the leading exponents. FIG. 4 plots the asymptotic exponents compared to the statistics of the  
 353 FTCLEs calculated for each push forward step. It can be seen that as the push forward step is  
 354 increased, the mean FTCLEs approach the asymptotic values and the standard deviation decreases  
 355 for the leading growth rates. Since the finite-time and asymptotic growth rates are computed using  
 356 different methods, this agreement provides confidence in the accuracy of the CLV calculation.

357 To quantify the total transient growth at each time step in an asymptotically stable system, we  
 358 use a finite-time dimension measure as introduced in Quinn et al. (2020). As a first step we reorder

359 the FTCLEs as

$$\max(\Lambda_i(t)) > \cdots > \min(\Lambda_i(t)) = \tilde{\Lambda}_1(t) > \cdots > \tilde{\Lambda}_N(t). \quad (15)$$

360 Then the finite-time dimension measure is given as

$$\dim_{KY}(t) = j + \frac{\sum_{i=1}^j \tilde{\Lambda}_i(t)}{|\tilde{\Lambda}_{j+1}(t)|}, \quad (16)$$

361 where

$$\sum_{i=1}^j \tilde{\Lambda}_i(t) \geq 0 \quad \text{and} \quad \sum_{i=1}^{j+1} \tilde{\Lambda}_i(t) < 0.$$

362 It is important to note that the sums of the FTCLEs do not relate to typical expansion and contraction  
 363 of volumes in tangent space as the CLVs are not necessarily orthogonal (Kuptsov and Kuznetsov  
 364 2018). The individual FTCLEs give the specific expansion and contraction of the tangent vectors,  
 365 and the finite-time dimension measure Eq. (16) defined as the local Kaplan-Yorke dimension is  
 366 being used here as an approximate measure of the number of unstable and near-neutral FTCLEs.

367 We next compare the probability of the occurrence of a positive dimension across all push  
 368 forward steps. The short push forward of  $M = 3$  shows the most unstable behavior, with 73% of  
 369 time instances associated with positive FTCLEs. The largest probability of occurrence is in the  
 370 negative NAO state with 99% of days assigned to that state experiencing a positive FTCLE. This is  
 371 followed by the positive NAO state at 62% and then the Atlantic Ridge at 39%. The probabilities  
 372 of observing a positive FTCLE starkly drops for the longer push forwards  $M = 10, 30, 50$  with all at  
 373 less than 1% regardless of state. This suggests that the instabilities within this model are associated  
 374 with fast-scale dynamics that are filtered out when using longer push forward lengths. On short  
 375 time scales the model is unstable the majority of the time, while on long time scales the stable  
 376 dynamics of the model dominate.

377 For the  $M = 3$  case exhibiting the most unstable behavior, we are interested in characterizing  
 378 stability based on the finite-time dimension,  $\overline{\dim_{KY}(t)}$ , averaged over residency in each state as

379 shown in TABLE 4. We see that the  $\text{NAO}^-$  state shows the most unstable behavior, followed by  
380 the  $\text{NAO}^+$  and then the AR state. To filter out periods of rapid transitioning, we also consider  
381 the average dimension of persistent states. Here we use a 5-day filter in which we include in the  
382 average only days where the model was in the state both 2 days before and 2 days following the day  
383 on which the dimension was calculated. When only persistent events are considered, the AR state  
384 experiences no unstable behavior, while the average dimension has increased slightly for both NAO  
385 phases. This is in agreement with previous studies that show blocking events (typically associated  
386 with a negative NAO phase) tend to have higher instantaneous instability than times of strong zonal  
387 flow (typically associated with the positive NAO phase) (Schubert and Lucarini 2016; Faranda  
388 et al. 2016, 2017; Lucarini and Gritsun 2020).

389 Since the FTCLs correspond to the growth and decay rates of particular CLVs, we can identify  
390 the modes which experience finite-time growth in each persistent state. Given that the average  
391  $\text{dim}_{KY}(t)$  measure is 0 in the AR state we can conclude there is no growing mode during long  
392 residencies in that state. For both the  $\text{NAO}^-$  and the  $\text{NAO}^+$  state there is only one unstable mode  
393 that contributes to the positive  $\text{dim}_{KY}(t)$  measure. To visualize what these modes look like in  
394 physical space, we take a projection of the CLVs onto the corresponding EOFs (appendix A). The  
395 resulting patterns are shown in FIG. 5. For the  $\text{NAO}^-$  state the instability arises in CLV 1 and  
396 projects as the NAO pattern itself, with a larger magnitude anomaly to the southeast of Greenland  
397 and an opposite, smaller magnitude anomaly south of that stretching from the east coast of North  
398 America to Spain. We see a similar pattern emerging in CLV 2 for the  $\text{NAO}^+$  state, with the northern  
399 anomaly stretching west into the northern parts of Canada and having a smaller magnitude.

400 We are also interested in the unstable CLVs around transitions and whether or not the patterns are  
401 distinct from those in FIG. 5. We first identify all transitions associated with persistent states, i.e.,  
402 residencies of greater than 4 days both before and after the transition. For this residency length and

403 a push forward of  $M = 3$  days, each of the 6 distinct transitions will have the same progression of  
404 dynamics each time the model experiences that particular transition. We show these 6 progressions  
405 of CLV patterns, FTCLEs, and alignment (introduced in the next section) in appendix D. While  
406 these transitions between persistent states account for some 921 days with unstable exponents over  
407 the full fit period, we find that this corresponds to only a few dozen distinct, recurring unstable  
408 patterns. By further classifying the observed patterns using the pattern correlation between CLVs,  
409 we determine four distinct modes that experience finite-time growth around the time of a transition  
410 (shown in FIG. 6). The main feature of all of these unstable modes compared to the unstable modes  
411 within the persistent states is more zonally oriented anomalous pressure gradients. TABLE 5 lists  
412 the transitions in which each pattern occurs, the day on which it occurs, the CLV number and  
413 associated FTCLE value. Patterns A and B appear only in transitions from the  $\text{NAO}^-$  state, pattern  
414 C only appears in transitions from the  $\text{NAO}^+$  to the AR state, and pattern D appears in both  $\text{NAO}^-$   
415 to  $\text{NAO}^+$  and  $\text{NAO}^+$  to  $\text{NAO}^-$  transitions. In terms of the CLVs in which the unstable patterns  
416 are expressed, patterns B and C are solely associated with CLV 2, pattern D is solely associated  
417 with CLV 1, and pattern A occurs in both CLVs 1 and 2. All unstable patterns occur either on  
418 the first or second day the model is in the end state of the transition. We note here that none of  
419 these patterns occur in transitions from the AR state. In those two cases the transition is marked by  
420 the emergence of the unstable persistent patterns in FIG. 5 in either CLV 1 or 2 as dictated by the  
421 end state. The CLV patterns associated with transitions to and from the respective NAO states are  
422 associated with either the formation or decay of the meridionally oriented structures characteristic  
423 of the respective NAO phases.

424 *b. Alignment of CLVs*

425 While the FTCLEs give the relative growth and decay rates of tangent vectors to the subspaces,  
 426 the angle between the CLVs (otherwise known as alignment) gives an idea of transversality of  
 427 the subspaces (Kuptsov and Kuznetsov 2018). High alignment of CLVs, or a vanishing angle  
 428 between subspaces, has been suggested to be an indicator of transitions and catastrophic events  
 429 (Beims and Gallas 2016; Sharafi et al. 2017). We measure the alignment of two CLVs through  
 430  $\theta_{i,j} = |\cos(\Theta_{i,j})|$  where  $\Theta_{i,j}$  is the angle between the  $i$ -th and  $j$ -th CLV. Values of  $\theta_{i,j}$  close to  
 431 one imply high alignment of the CLVs, while values close to zero imply orthogonality. Here we  
 432 calculate the alignment using the following:

$$\theta_{i,j}(t) = \frac{|\phi_i(t) \cdot \phi_j(t)|}{\|\phi_i(t)\| \cdot \|\phi_j(t)\|}. \quad (17)$$

433 We first consider the alignment of the CLVs calculated for the short push forward step ( $M = 3$ ).  
 434 FIG. 7 shows the alignment of the leading CLVs ( $\theta_{1,2}$ ,  $\theta_{2,3}$ , and  $\theta_{1,3}$ ) for two different time  
 435 segments; we also plot the leading growth rates ( $\Lambda_1$ ,  $\Lambda_2$ , and  $\Lambda_3$ ), dimension, and state indicators  
 436 for comparison. We indeed see a spike in the alignment values around the time of transitions,  
 437 with the most prominent spikes typically in  $\theta_{1,2}$  and  $\theta_{2,3}$ . The differing behavior of dimension  
 438 by state discussed in section 3a can be seen clearly in the two figures. FIG. 7a shows an example  
 439 segment which has long residencies in the  $\text{NAO}^-$  state. We see that for long enough residencies  
 440 the dimension measure remains around 3 with the driving instability coming from the first CLV.  
 441 On the contrary, residencies longer than two days in the AR state show the dimension measure  
 442 quickly dropping to zero. This is further illustrated in FIG. 7b where the model resides primarily in  
 443 the AR and  $\text{NAO}^+$  state. The lower dimension measures are driven by the differing behavior of  $\Lambda_1$   
 444 which remains close to  $\Lambda_2$  and both oscillate around zero. We see that for long enough residency  
 445 in the  $\text{NAO}^+$  state the instability is driven by  $\Lambda_2$  overtaking  $\Lambda_1$ .

446 In order to obtain a more complete understanding of the alignment behavior around transitions,  
 447 FIG. 8 shows the collective alignment values centered around the days associated with transition  
 448 (filtered for state residencies longer than 4 days before and after the transition). The transition  
 449 occurs from day 0 to day 1. The greatest change in behavior can be seen on days 0, 1, and 2 for  
 450  $\theta_{1,2}$ , and days 1 and 2 for  $\theta_{2,3}$  and  $\theta_{1,3}$ . The most noticeable change is in the increased values of the  
 451 third quartile and the maximum. The leading alignment  $\theta_{1,2}$  shows an overall increase in alignment  
 452 values on day 1 and 2 for all transitions. There is also an increase in the median value preceding  
 453 the transitions on day  $-1$ . The increased spread of alignment around transitions is due to differing  
 454 alignment behavior for each type of transition as can be seen in FIG. 7. We therefore separate the  
 455 alignment behavior by specific transition and plot the ensemble of trajectories in FIG. 9. We see  
 456 that transitions from the  $\text{NAO}^-$  state show an increase in  $\theta_{1,2}$  on the days preceding the transition.  
 457 The peak in  $\theta_{1,2}$  occurs on the last day the affiliation sequence is in the preceding state. We also  
 458 observe that there is a spike in  $\theta_{2,3}$  following both transitions from the  $\text{NAO}^-$  state; for  $\text{NAO}^-$   
 459 to AR it occurs on the day following the peak in  $\theta_{1,2}$  and for  $\text{NAO}^-$  to  $\text{NAO}^+$  it occurs two days  
 460 following. For both transitions from the  $\text{NAO}^+$  state there is an increase in  $\theta_{1,2}$ ,  $\theta_{2,3}$ , and  $\theta_{1,3}$ ,  
 461 with the maximum values for each occurring two days after the transitions. For the AR to  $\text{NAO}^+$   
 462 transition there is an increase in  $\theta_{2,3}$  with a peak on the day just following the transition. The other  
 463 two alignments ( $\theta_{1,2}$  and  $\theta_{1,3}$ ) also show a weak increase. The AR to  $\text{NAO}^-$  transition shows the  
 464 overall weakest signal in alignment, although all three still display an increase within two days of  
 465 the transition.

466 Next we consider the behavior of the alignment of the leading two CLVs,  $\theta_{1,2}(t)$ , across the  
 467 varying push forward lengths. This is displayed in the panels of FIG. 10a. The first difference  
 468 we notice is in the timescale of variability of the alignment. For shorter push forward lengths we  
 469 observe that large changes in alignment occur more often than for longer push forward lengths. We

470 also observe the emergence of a low-frequency signal within the variability as the push forward  
471 length is increased. To explore the emergence of this signal we compute the power spectral  
472 density (PSD) of each alignment time series. The PSDs are shown in FIG. 10b, scaled to show  
473 the frequency percentage contribution to variance. The red dots show the peaks that are identified  
474 using a threshold of 2 standard deviations away from neighboring measures, while the red crosses  
475 use a threshold of 3 standard deviations. We can see the emergence of a significant low-frequency  
476 signal for the push forward length of 30 days or longer. This frequency corresponds to a period of  
477 approximately 1 year.

478 We relate the annual signal emerging in the alignment of the leading CLVs to the seasonality of  
479 the NAO. A study of the NAO in both observational data and reanalysis products has shown that  
480 there is increased variability in the NAO index in the boreal winter and decreased average NAO  
481 values in the boreal summer (Hanna et al. 2015). To measure relative variability in the NAO index  
482 for our model we define a transition index,

$$\text{Transition index} = \sum_{i=t-50}^t \frac{\mathbb{I}_{\text{tran}}(i)}{50}. \quad (18)$$

483 Here  $\mathbb{I}_{\text{tran}}(i)$  is again the indicator function for a transition occurring at time  $i$ , and we choose a  
484 window of 50 days to match the longest push forward step used to calculate alignment. The time  
485 series of the transition index compared to  $\theta_{1,2}$  for  $M = 50$  is shown in FIG. 11. We observe that the  
486 two measures are anti-correlated. The maximum Pearson correlation coefficient is  $-0.45$  at a 17  
487 day lag with the alignment. The transition index also shows a peak in its PSD corresponding to an  
488 annual signal (not shown).

489 While FIG. 11 compares the alignment and NAO variability in time, we are also interested in the  
490 average behavior by season. The various NAO indices computed from both observational records  
491 and reanalysis products have been shown to exhibit distinct seasonal behavior. In a study by Hanna



492 et al. (2015) the authors analyze a collection of station-based data and reanalyses and compare  
493 seasonal differences as well as trends. They find that there has been increased variability in the  
494 NAO during the boreal winter (DJF), particularly in December, throughout the last century. The  
495 authors also noted a decrease in boreal summer (JJA) NAO values over the past 20-30 years. To  
496 analyze how the seasonality of our model compares, we consider the total number of transitions  
497 and days spent in a given state each season as shown in TABLE 2. The seasonality in the  $\text{NAO}^-$  state  
498 is seen more through the total number of days spent in a given state and average residency times.  
499 As mentioned in section 2c, the  $\text{NAO}^-$  state accounts for 46.5% of the total number of model days.  
500 The largest contribution to that comes from JJA (41%) compared to DJF which only accounts for  
501 11% of  $\text{NAO}^-$  days. This seasonality is similar to, but much more pronounced than, that observed  
502 for the CPC NAO index; over the same period as the model fit, 45% of days had a negative daily  
503 mean index, and 20% of these days occurred during DJF compared to 29% accounted for by JJA.  
504 The average residency length also has a seasonal signal (TABLE 1), with its maximum in JJA (9.3  
505 days) and minimum in DJF (2.5 days). We observe as expected a seasonal signal in the transition  
506 probabilities, with the highest probability of a transition occurring in SON (30%), while JJA has  
507 the lowest overall probability of transitions (15%). When we separate by the state associated with  
508 each transition, we see different seasonal behavior across the three states. Transitions associated  
509 with the  $\text{NAO}^-$  state have roughly the same probability of occurring in DJF as in the JJA (16%).  
510 Those probabilities are lower than what is seen in MAM (23%) and SON (24%) which are generally  
511 referred to as transitional seasons. On the contrary, the transitions associated solely with the  $\text{NAO}^+$   
512 and Atlantic Ridge states have a much stronger seasonal signal. The probability is nine times higher  
513 in DJF (18%) than in JJA (2%) for transitions between the  $\text{NAO}^+$  and AR states which contributes  
514 to the overall increase in DJF variability compared to JJA.

515 We now turn to the average behavior of alignment by season. FIG. 12 shows the alignment  
516 averaged over each season of the indicated pairs of CLVs. We see a clear seasonal behavior of  $\theta_{1,2}$   
517 with a maximum in summer and a minimum in autumn and winter. Interestingly, there is also a  
518 seasonal signal in  $\theta_{2,3}$ ,  $\theta_{2,4}$  and  $\theta_{3,4}$  (although weaker for  $\theta_{2,4}$  and  $\theta_{3,4}$ ). We do not see a seasonal  
519 cycle in the alignments with the more asymptotically stable CLVs (5-7) as their dominant signals  
520 have a cycle length of less than a year.

#### 521 **4. Summary**

522 We have presented here a dynamical analysis of a reduced model for the NAO teleconnection.  
523 The preferred model has been constructed through application of the FEM-BV-VAR method which  
524 has been previously used to identify atmospheric pressure states consistent with known coherent  
525 features in the North Atlantic (Risbey et al. 2015; O’Kane et al. 2017). The identified states  
526 are also consistent with an alternate FEM-BV-EOF (Franzke et al. 2009) variant analysis. Using  
527 the NCEP/NCAR Reanalysis 1 (Kalnay et al. 1996) from 1979 to 2018, we tested a range of  
528 hyperparameters to determine an optimal model. The resulting optimal model was found to be  
529 non-Markovian with a time dependence (memory) of 3 days, an average state length of 5 days,  
530 and 3 cluster states. The cluster states closely resemble the two phases of the NAO and a pattern  
531 similar to the AR.

532 In order to study the time-dependent model dynamics, we constructed a non-smooth linear  
533 mapping system defined on a delay-embedding of the PCs. The non-smooth switching is defined  
534 a priori by the affiliation sequence resulting from the FEM-BV-VAR fit. Through this novel way  
535 of constructing the system we were able to analyze the time-dependent tangent linear propagator,  
536 calculating the CLVs, their finite-time growth and decay rates, and their alignment. We differentiate

537 between short time-scale dynamics and long time-scale dynamics by using different window lengths  
538 over which to calculate the CLVs.

539 While the individual states are asymptotically stable, on short time-scales they can exhibit finite-  
540 time growth. In particular, we found that both NAO states contain finite-time unstable CLVs  
541 for a window length of 3 days, with the NAO<sup>-</sup> state showing stronger instability than the NAO<sup>+</sup>  
542 state. We used a finite-time dimension measure to characterize the instability and identified the  
543 largest dimension to be associated with the blocked NAO<sup>-</sup> state, which is consistent with recent  
544 studies of blocking in theoretical models (Schubert and Lucarini 2016) and data (Faranda et al.  
545 2017; Lucarini and Gritsun 2020). We next projected the unstable CLVs into physical space in  
546 order to visualize the pressure anomaly patterns associated with the finite-time growth. During  
547 persistent states the instability manifests as an NAO-like meridional pressure gradient, whereas  
548 around transitions between persistent states the instability manifests in more zonally oriented  
549 pressure gradient patterns.

550 The alignment of the CLVs also showed different behavior on short versus long time-scales.  
551 On short time-scales (window length of 3 days) there was an increase in alignment of the leading  
552 CLVs around the time of transitions. The increase occurred anywhere between the last day of the  
553 preceding state and the second day of the end state. For longer time-scales we observed starkly  
554 different behavior whereby a low-frequency signal in alignment emerged as the window length  
555 was increased, converging to an annual oscillation with a maximum in the boreal summer (JJA)  
556 and a minimum in the boreal winter (DJF) at windows of 30 plus days. A transition index, defined  
557 over the same window length, was computed to characterize the tendency of the model to switch  
558 between states and found to be anti-correlated with the alignment and have a pronounced annual  
559 signal. The seasonality in alignment was also related to the seasonality seen in the NAO<sup>-</sup> average  
560 residency length and model preference for different states in JJA versus DJF.

561 The novel dynamical systems analysis of a data-driven model of the NAO presented here is  
562 general and does not have to be restricted to this particular phenomenon nor to atmospheric  
563 teleconnection studies. One could perform a similar analysis on any resulting model from the  
564 use of the FEM-BV-VAR clustering method or general reduced order stochastic models. With  
565 respect to atmospheric and oceanic teleconnections, this method provides a way of extracting the  
566 large-scale unstable perturbation directions associated with specific phenomena. Future studies  
567 will aim to characterize the behavior of other teleconnection interactions as well as anomalous  
568 events associated with particular large-scale atmospheric modes.

569 *Acknowledgments.* CQ and TO are supported by the Australian Commonwealth Scientific  
570 and Industrial Research Organisation (CSIRO) Decadal Climate Forecasting Project (<https://research.csiro.au/dfp>)  
571 (<https://research.csiro.au/dfp>). DH is supported by the CSIRO  
572 through a ResearchPlus postdoctoral fellowship. The EOF analysis was implemented using the  
573 scikit-learn Python package (Pedregosa et al. 2011), and plots were generated using the Python  
574 package Matplotlib (Hunter 2007).

575 *Data availability statement.* The NCEP/NCAR reanalysis output used is provided by the  
576 NOAA/OAR/ESRL PSL, Boulder, Colorado, USA, and may be accessed at <https://psl.noaa.gov/data/reanalysis/reanalysis.shtml>. All source code used to perform the analyses  
577 presented in this study may be found at <https://doi.org/10.5281/zenodo.4035644>.

## 579 APPENDIX A

### 580 EOFs of North Atlantic Region

581 Figure A1 shows the EOFs used in the dimension reduction applied to the NCEP/NCAR Reanal-  
582 ysis 1 atmospheric pressure anomaly data from the base period 1 January 1979 to 31 December

583 2018. In calculating the EOFs and corresponding PCs, the data is weighted by the square root of  
584 the cosine of the latitude. We use a truncated singular value decomposition for 200 components  
585 and a unit normalization for the EOFs. The 20 EOFs displayed in Figure A1 account for 91% of  
586 the total variance, and EOF 1 resembles the typical NAO pattern.

## 587 APPENDIX B

### 588 **Minimization of FEM-BV-VAR loss function**

589 In general, direct minimization of Eq. (2) with the component losses given by Eq. (6) to find the  
590 optimal affiliations  $\Gamma$  and parameters  $\Theta$  is not practical. However, the loss function is separately  
591 convex in  $\Gamma$  and  $\Theta$ , and approximate minimizers  $(\hat{\Gamma}, \hat{\Theta})$  may be straightforwardly computed by  
592 alternately minimizing Eq. (2) with respect to  $\Gamma$  for fixed  $\Theta$  and vice versa, until convergence  
593 is reached. The minimization problem with respect to  $\Gamma$  for fixed  $\Theta$  may be formulated as a  
594 constrained linear programming problem (Metzner et al. 2012) and solved numerically. For fixed  
595  $\Gamma$ , the optimal parameters  $\Theta_i$  are given by weighted least-squares estimates. In terms of the matrices

$$\begin{aligned}
\mathbf{X} &= (\mathbf{x}_{m_{\max}+1}, \dots, \mathbf{x}_T) \in \mathbb{R}^{d \times (T-m_{\max})}, \\
\mathbf{Z} &= \begin{pmatrix} 1 & \dots & 1 \\ \mathbf{x}_{m_{\max}} & \dots & \mathbf{x}_{T-1} \\ \vdots & \dots & \vdots \\ \mathbf{x}_{m_{\max}-m} & \dots & \mathbf{x}_{T-m} \end{pmatrix} \in \mathbb{R}^{(1+md) \times (T-m_{\max})}, \\
\mathbf{W}_i &= \text{diag}([\gamma_{m_{\max}+1}]_i, \dots, [\gamma_T]_i) \in \mathbb{R}^{(T-m_{\max}) \times (T-m_{\max})}, \\
\mathbf{B}_i &= (\boldsymbol{\mu}^{(i)}, \mathbf{A}_1^{(i)}, \dots, \mathbf{A}_m^{(i)}) \in \mathbb{R}^{d \times (1+md)},
\end{aligned}$$

596 the estimated parameters for state  $i$  at fixed  $\mathbf{\Gamma}$  may be compactly written as

$$\begin{aligned}\hat{\mathbf{B}}_i &= \mathbf{X}\mathbf{W}_i\mathbf{Z}^T \left( \mathbf{Z}\mathbf{W}_i\mathbf{Z}^T \right)^{-1}, \\ \hat{\Sigma}^{(i)} &= \frac{1}{\text{Tr}[\mathbf{W}_i]} (\mathbf{X} - \hat{\mathbf{B}}_i\mathbf{Z})\mathbf{W}_i(\mathbf{X} - \hat{\mathbf{B}}_i\mathbf{Z})^T,\end{aligned}\tag{B1}$$

597 where  $\text{Tr}[\mathbf{A}]$  denotes the trace of a matrix  $\mathbf{A}$ . This coordinate descent method finds a local minimum  
598 of the loss function for a given initial guess at the optimal parameters and not necessarily a globally  
599 optimal solution. In order to reduce the degree to which this occurs, in all of the results presented  
600 we run the optimization  $N_{\text{init}} = 20$  times with different initial guesses and keep the solution with  
601 the lowest loss.

602 To select a single set of values for the hyperparameters  $K$ ,  $m$ , and  $p$ , we use the following  
603 cross-validation method. The observed sample is divided into  $N_{\text{fold}} + 1$  approximately equal length  
604 segments  $\mathcal{T}_1, \dots, \mathcal{T}_{N_{\text{fold}}+1}$ , and each model is refit  $N_{\text{fold}}$  times, where on the  $i^{\text{th}}$  iteration the first  
605  $i$  segments are used as the training sample. Holding the obtained state parameters  $\hat{\Theta}$  fixed, the  
606 optimal affiliations are calculated by minimizing the cost function evaluated over the  $(i + 1)^{\text{th}}$   
607 segment, adjusting the upper bound  $C_T$  as appropriate for the length of the segment with fixed  $p$ .

608 The weighted root mean square error

$$\text{RMSE}_i = \sqrt{\frac{1}{d(T_i - m_{\text{max}})} \sum_{t \in \mathcal{T}_{i+1}} \sum_{j=1}^K [\gamma_t]_j \left\| \mathbf{x}_t - \hat{\mathbf{x}}_t^{(j)} \right\|^2}$$

609 is then evaluated for each test segment, where  $\hat{\mathbf{x}}_t^{(j)}$  denotes the expected value under state  $j$ . The  
610 mean reconstruction RMSE over the set of test sets provides a measure of the model's ability to  
611 generalize to future data, which we use in lieu of estimates of out-of-sample prediction error, with  
612 good performance on this measure involving a compromise between model flexibility and overfitting  
613 the training data. We note that the more standard cross-validation approach, that is estimation of  
614 the out-of-sample forecast error, would require an additional model for the dynamics of the hidden  
615 switching process, which we here leave to future work. Alternatively, in-sample measures based on

616 information criteria could be used when combined with an appropriate likelihood model. However,  
617 this similarly requires an appropriate probabilistic model to be specified for the switching and noise  
618 processes, and, moreover, the very large number of estimated degrees of freedom in comparison  
619 to the available sample size may lead to concerns as to their suitability (Burnham and Anderson  
620 2002).

## 621 APPENDIX C

### 622 QR decomposition method

623 The QR algorithm we use for computing the asymptotic Lyapunov exponents follows Dieci et al.  
624 (1997). It is based on the numerical linear algebra factorisation of a matrix into an orthogonal  
625 matrix  $\mathbf{Q}$  and an upper triangular matrix  $\mathbf{R}$ . The initial arbitrary orthogonal matrix can be set as  
626  $\mathbf{Q}_0 = \mathbf{I}_N$  where  $\mathbf{I}$  is the identity matrix and  $N$  is the number of states in the state space. We then  
627 define the  $\mathbf{Q}_i$  and  $\mathbf{R}_i$  matrices iteratively through the QR decomposition of  $\mathbf{A}_i \mathbf{Q}_{i-1}$ :

$$\mathbf{Q}_i \mathbf{R}_i = \mathbf{A}_i \mathbf{Q}_{i-1}, \quad (\text{C1})$$

628 where  $\mathbf{A}_i = \mathcal{A}(t_i, 0)$ , our matrix cocycle defined by Eq. (11). The upper triangular matrix  $\mathbf{R}_i$  holds  
629 the eigenvalues  $R_{i,jj} > 0$  where  $j$  indicates the position of the matrix entry. After  $T$  time steps we  
630 have the equivalence

$$\mathbf{Q}_T \mathbf{R}_T \dots \mathbf{R}_1 = \mathbf{A}_T \dots \mathbf{A}_1 \mathbf{Q}_0. \quad (\text{C2})$$

631 We then approximate the asymptotic Lyapunov exponents through

$$\lambda_j = \frac{1}{T} \sum_{i=1}^T \ln R_{i,jj} \quad \text{for } j = 1, \dots, N. \quad (\text{C3})$$

## APPENDIX D

### CLV patterns for transitions associated with persistent states

We show the leading CLV patterns during each of the six transitions associated with persistent states: AR to NAO<sup>-</sup> (FIG. D1), AR to NAO<sup>+</sup> (FIG. D2), NAO<sup>-</sup> to AR (FIG. D3), NAO<sup>-</sup> to NAO<sup>+</sup> (FIG. D4), NAO<sup>+</sup> to AR (FIG. D5), NAO<sup>+</sup> to NAO<sup>-</sup> (FIG. D6). The transition occurs between Day 0 and 1, and we show the three days preceding and the 3 days following. Due to the filtering on persistent states (minimum of 5 days in each state on either side of the transition), Days -2 and 3 show the CLV patterns associated with the stationary states before and after the transition, respectively. The top two panels in each figure indicate the associated alignment and FTCLE behavior. Note that we only show  $\Lambda_1$  and  $\Lambda_2$  as  $\Lambda_3$  is always negative in these cases.

### References

- Barnston, A. G., and R. E. Livezey, 1987: Classification, Seasonality and Persistence of Low-Frequency Atmospheric Circulation Patterns. *Monthly Weather Review*, **115** (6), 1083–1126, doi:10.1175/1520-0493(1987)115<1083:CSAPOL>2.0.CO;2.
- Beims, M. W., and J. A. Gallas, 2016: Alignment of lyapunov vectors: A quantitative criterion to predict catastrophes? *Scientific reports*, **6** (1), 1–7, doi:10.1038/srep37102.
- Benedict, J. J., S. Lee, and S. B. Feldstein, 2004: Synoptic view of the north atlantic oscillation. *Journal of the Atmospheric Sciences*, **61** (2), 121–144, doi:10.1175/1520-0469(2004)061%3C0121:SVOTNA%3E2.0.CO;2.
- Burnham, K. P., and D. R. Anderson, 2002: *Model Selection and Multimodel Inference*. 2nd ed., Springer.



- 653 Cassou, C., 2008: Intraseasonal interaction between the madden–julian oscillation and the north  
654 atlantic oscillation. *Nature*, **455 (7212)**, 523–527, doi:10.1038/nature07286.
- 655 Cassou, C., L. Terray, and A. S. Phillips, 2005: Tropical Atlantic Influence on European Heat  
656 Waves. *Journal of Climate*, **18 (15)**, 2805–2811, doi:10.1175/JCLI3506.1.
- 657 Cheng, X., and J. M. Wallace, 1993: Cluster Analysis of the Northern Hemisphere Wintertime 500-  
658 hPa Height Field: Spatial Patterns. *Journal of the Atmospheric Sciences*, **50 (16)**, 2674–2696,  
659 doi:10.1175/1520-0469(1993)050<2674:CAOTNH>2.0.CO;2.
- 660 Cleveland, W. S., 1979: Robust locally weighted regression and smoothing scatterplots. *Jour-  
661 nal of the American Statistical Association*, **74 (368)**, 829–836, doi:10.1080/01621459.1979.  
662 10481038.
- 663 Croci-Maspoli, M., C. Schwierz, and H. C. Davies, 2007: Atmospheric blocking: Space-time links  
664 to the nao and pna. *Climate Dynamics*, **29 (7-8)**, 713–725, doi:10.1007/s00382-007-0259-4.
- 665 Crommelin, D. T., 2004: Observed Nondiffusive Dynamics in Large-Scale Atmospheric Flow.  
666 *Journal of the Atmospheric Sciences*, **61 (19)**, 2384–2396, doi:10.1175/1520-0469(2004)  
667 061<2384:ONDILA>2.0.CO;2.
- 668 Dieci, L., R. D. Russell, and E. S. Van Vleck, 1997: On the computation of lyapunov exponents  
669 for continuous dynamical systems. *SIAM journal on numerical analysis*, **34 (1)**, 402–423, doi:  
670 10.1137/S0036142993247311.
- 671 Falkena, S. K., J. de Wiljes, A. Weisheimer, and T. G. Shepherd, 2020: Revisiting the identification  
672 of wintertime atmospheric circulation regimes in the euro-atlantic sector. *Quarterly Journal of  
673 the Royal Meteorological Society*, 1–14, doi:10.1002/qj.3818.

- 674 Faranda, D., G. Masato, N. Moloney, Y. Sato, F. Daviaud, B. Dubrulle, and P. Yiou, 2016: The  
675 switching between zonal and blocked mid-latitude atmospheric circulation: a dynamical system  
676 perspective. *Climate Dynamics*, **47 (5-6)**, 1587–1599, doi:10.1007/s00382-015-2921-6.
- 677 Faranda, D., G. Messori, and P. Yiou, 2017: Dynamical proxies of north atlantic predictability and  
678 extremes. *Scientific reports*, **7**, 41 278, doi:10.1038/srep41278.
- 679 Feldstein, S. B., 2003: The dynamics of nao teleconnection pattern growth and decay. *Quarterly*  
680 *Journal of the Royal Meteorological Society*, **129 (589)**, 901–924, doi:10.1256/qj.02.76.
- 681 Fereday, D., 2017: How Persistent Are North Atlantic–European Sector Weather Regimes? *Journal*  
682 *of Climate*, **30 (7)**, 2381–2394, doi:10.1175/JCLI-D-16-0328.1.
- 683 Fereday, D. R., J. R. Knight, A. A. Scaife, C. K. Folland, and A. Philipp, 2008: Cluster Analysis  
684 of North Atlantic–European Circulation Types and Links with Tropical Pacific Sea Surface  
685 Temperatures. *Journal of Climate*, **21 (15)**, 3687–3703, doi:10.1175/2007JCLI1875.1.
- 686 Franzke, C., D. Crommelin, A. Fischer, and A. J. Majda, 2008: A Hidden Markov Model Perspec-  
687 tive on Regimes and Metastability in Atmospheric Flows. *Journal of Climate*, **21 (8)**, 1740–1757,  
688 doi:10.1175/2007JCLI1751.1.
- 689 Franzke, C., I. Horenko, A. J. Majda, and R. Klein, 2009: Systematic Metastable Atmospheric  
690 Regime Identification in an AGCM. *Journal of the Atmospheric Sciences*, **66 (7)**, 1997–2012,  
691 doi:10.1175/2009JAS2939.1.
- 692 Franzke, C., S. Lee, and S. B. Feldstein, 2004: Is the North Atlantic Oscillation a Breaking Wave?  
693 *Journal of the Atmospheric Sciences*, **61 (2)**, 145–160, doi:10.1175/1520-0469(2004)061<0145:  
694 ITNAOA>2.0.CO;2.

- 695 Franzke, C. L. E., T. J. O’Kane, D. P. Monselesan, J. S. Risbey, and I. Horenko, 2015: Systematic  
696 attribution of observed southern hemisphere circulation trends to external forcing and internal  
697 variability. *Nonlinear Processes in Geophysics*, **22 (5)**, 513–525, doi:10.5194/npg-22-513-2015.
- 698 Franzke, C. L. E., T. Woolins, and O. Martius, 2011: Persistent Circulation Regimes and Preferred  
699 Regime Transitions in the North Atlantic. *Journal of the Atmospheric Sciences*, **68 (12)**, 2809–  
700 2825, doi:10.1175/JAS-D-11-046.1.
- 701 Frederiksen, J., 2002: Genesis of intraseasonal oscillations and equatorial waves. *Journal*  
702 *of the Atmospheric Sciences*, **59 (19)**, 2761–2781., doi:10.1175/1520-0469(2002)059<2761:  
703 GOIOAE>2.0.CO;2.
- 704 Frederiksen, J., and C. Frederiksen, 1993: Monsoon disturbances, intraseasonal oscillations,  
705 teleconnection patterns, blocking, and storm tracks of the global atmosphere during January  
706 1979: Linear theory. *Journal of the Atmospheric Sciences*, **50 (10)**, 1349–1372, doi:10.1175/  
707 1520-0469(1993)050<1349:MDIOTP>2.0.CO;2.
- 708 Frederiksen, J., and H. Lin, 2013: Tropical-Extratropical Interactions of Intraseasonal Oscillations.  
709 *Journal of the Atmospheric Sciences*, **70 (10)**, 3180–3197., doi:10.1175/JAS-D-12-0302.1.
- 710 Froyland, G., T. Hüls, G. P. Morriss, and T. M. Watson, 2013: Computing covariant lyapunov  
711 vectors, oseledets vectors, and dichotomy projectors: A comparative numerical study. *Physica*  
712 *D: Nonlinear Phenomena*, **247 (1)**, 18–39, doi:10.1016/j.physd.2012.12.005.
- 713 Ginelli, F., P. Poggi, A. Turchi, H. Chaté, R. Livi, and A. Politi, 2007: Characterizing dynamics with  
714 covariant lyapunov vectors. *Phys. Rev. Lett.*, **99**, 130 601, doi:10.1103/PhysRevLett.99.130601.
- 715 Hanna, E., T. E. Cropper, P. D. Jones, A. A. Scaife, and R. Allan, 2015: Recent seasonal asymmetric  
716 changes in the nao (a marked summer decline and increased winter variability) and associated

- 717 changes in the ao and greenland blocking index. *International Journal of Climatology*, **35** (9),  
718 2540–2554, doi:10.1002/joc.4157.
- 719 Hannachi, A., and B. Legras, 1995: Simulated annealing and weather regimes classification. *Tellus*  
720 *A*, **47** (5), 955–973, doi:10.1034/j.1600-0870.1995.00203.x.
- 721 Harries, D., and T. J. O’Kane, 2020: Applications of matrix factorization methods to climate data.  
722 *Nonlinear Processes in Geophysics*, **27** (3), 453–471, doi:10.5194/npg-27-453-2020.
- 723 Horenko, I., 2009: On robust estimation of low-frequency variability trends in discrete markovian  
724 sequences of atmospheric circulation patterns. *Journal of the atmospheric sciences*, **66** (7),  
725 2059–2072, doi:10.1175/2008JAS2959.1.
- 726 Horenko, I., 2010a: On clustering of non-stationary meteorological time series. *Dynamics of*  
727 *Atmospheres and Oceans*, **49** (2-3), 164–187, doi:10.1016/j.dynatmoce.2009.04.003.
- 728 Horenko, I., 2010b: On the identification of nonstationary factor models and their application  
729 to atmospheric data analysis. *Journal of the Atmospheric Sciences*, **67** (5), 1559–1574, doi:  
730 10.1175/2010JAS3271.1.
- 731 Hunter, J. D., 2007: Matplotlib: A 2d graphics environment. *Computing in Science & Engineering*,  
732 **9** (3), 90–95, doi:10.1109/MCSE.2007.55.
- 733 Hurrell, J. W., 1995: Decadal trends in the north atlantic oscillation: Regional temperatures and  
734 precipitation. *Science*, **269** (5224), 676–679, doi:10.1126/science.269.5224.676.
- 735 Hurrell, J. W., Y. Kushnir, G. Ottersen, and M. Visbeck, 2013: *An Overview of the North Atlantic*  
736 *Oscillation*, 1–35. American Geophysical Union (AGU), doi:10.1029/134GM01.

- 737 Huth, R., C. Beck, A. Philipp, M. Demuzere, Z. Ustrnul, M. Cahynová, J. Kyselý, and O. E. Tveito,  
738 2008: Classifications of atmospheric circulation patterns. *Annals of the New York Academy of*  
739 *Sciences*, **1146 (1)**, 105–152, doi:10.1196/annals.1446.019.
- 740 Kalnay, E., and Coauthors, 1996: The ncep/ncar 40-year reanalysis project. *Bulletin of the Amer-*  
741 *ican meteorological Society*, **77 (3)**, 437–472, doi:10.1175/1520-0477(1996)077%3C0437:  
742 TNYRP%3E2.0.CO;2.
- 743 Kidson, J. W., 2000: An analysis of new zealand synoptic types and their use in defining  
744 weather regimes. *International Journal of Climatology*, **20 (3)**, 299–316, doi:10.1002/(SICI)  
745 1097-0088(20000315)20:3<299::AID-JOC474>3.0.CO;2-B.
- 746 Kimoto, M., and M. Ghil, 1993a: Multiple Flow Regimes in the Northern Hemisphere Winter.  
747 Part I: Methodology and Hemispheric Regimes. *Journal of the Atmospheric Sciences*, **50 (16)**,  
748 2625–2644, doi:10.1175/1520-0469(1993)050<2625:MFRITN>2.0.CO;2.
- 749 Kimoto, M., and M. Ghil, 1993b: Multiple Flow Regimes in the Northern Hemisphere Winter. Part  
750 II: Sectorial Regimes and Preferred Transitions. *Journal of the Atmospheric Sciences*, **50 (16)**,  
751 2645–2673, doi:10.1175/1520-0469(1993)050<2645:MFRITN>2.0.CO;2.
- 752 Kuptsov, P. V., and S. P. Kuznetsov, 2018: Lyapunov analysis of strange pseudohyperbolic attrac-  
753 tors: angles between tangent subspaces, local volume expansion and contraction. *Regular and*  
754 *Chaotic Dynamics*, **23 (7-8)**, 908–932, doi:10.1134/S1560354718070079.
- 755 Kuptsov, P. V., and U. Parlitz, 2012: Theory and computation of covariant lyapunov vectors.  
756 *Journal of nonlinear science*, **22 (5)**, 727–762, doi:10.1007/s00332-012-9126-5.

- 757 Legras, B., and M. Ghil, 1985: Persistent Anomalies, Blocking and Variations in Atmospheric Pre-  
758 dictability. *Journal of the Atmospheric Sciences*, **42** (5), 433–471, doi:10.1175/1520-0469(1985)  
759 042<0433:PABAVI>2.0.CO;2.
- 760 Lin, H., G. Brunet, and J. Derome, 2018: An Observed Connection between the North Atlantic  
761 Oscillation and the Madden-Julian (O)scillation. *Journal of Climate*, **22** (2), 364–380., doi:  
762 10.1175/2008JCLI2515.1.
- 763 Lucarini, V., and A. Gritsun, 2020: A new mathematical framework for atmospheric blocking  
764 events. *Climate Dynamics*, **54** (1-2), 575–598, doi:10.1007/s00382-019-05018-2.
- 765 Luo, D., and J. Cha, 2012: The North Atlantic Oscillation and the North Atlantic Jet Variability:  
766 Precursors to NAO Regimes and Transitions. *Journal of the Atmospheric Sciences*, **69** (12),  
767 3763–3787, doi:10.1175/JAS-D-12-098.1.
- 768 Luo, D., T. Gong, and Y. Diao, 2007a: Dynamics of Eddy-Driven Low-Frequency Dipole Modes.  
769 Part III: Meridional Displacement of Westerly Jet Anomalies during Two Phases of NAO. *Journal*  
770 *of the Atmospheric Sciences*, **64** (9), 3232–3248, doi:10.1175/JAS3998.1.
- 771 Luo, D., T. Gong, and A. R. Lupo, 2007b: Dynamics of Eddy-Driven Low-Frequency Dipole  
772 Modes. Part II: Free Mode Characteristics of NAO and Diagnostic Study. *Journal of the Atmo-*  
773 *spheric Sciences*, **64** (1), 29–51, doi:10.1175/JAS3820.1.
- 774 Luo, D., A. R. Lupo, and H. Wan, 2007c: Dynamics of Eddy-Driven Low-Frequency Dipole  
775 Modes. Part I: A Simple Model of North Atlantic Oscillations. *Journal of the Atmospheric*  
776 *Sciences*, **64** (1), 3–28, doi:10.1175/JAS3818.1.

- 777 Majda, A. J., C. L. Franzke, A. Fischer, and D. T. Crommelin, 2006: Distinct metastable at-  
778 mospheric regimes despite nearly gaussian statistics: A paradigm model. *Proceedings of the*  
779 *National Academy of Sciences*, **103 (22)**, 8309–8314, doi:10.1073/pnas.0602641103.
- 780 Metzner, P., L. Putzig, and I. Horenko, 2012: Analysis of persistent nonstationary time series  
781 and applications. *Communications in Applied Mathematics and Computational Science*, **7 (2)**,  
782 175–229, doi:10.2140/camcos.2012.7.175.
- 783 Michelangeli, P.-A., R. Vautard, and B. Legras, 1995: Weather Regimes: Recurrence and  
784 Quasi Stationarity. *Journal of the Atmospheric Sciences*, **52 (8)**, 1237–1256, doi:10.1175/  
785 1520-0469(1995)052<1237:WRRSQS>2.0.CO;2.
- 786 Mo, K., and M. Ghil, 1988: Cluster analysis of multiple planetary flow regimes. *Journal of*  
787 *Geophysical Research: Atmospheres*, **93 (D9)**, 10 927–10 952, doi:10.1029/JD093iD09p10927.
- 788 Molteni, F., S. Tibaldi, and T. N. Palmer, 1990: Regimes in the wintertime circulation over northern  
789 extratropics. i: Observational evidence. *Quarterly Journal of the Royal Meteorological Society*,  
790 **116 (491)**, 31–67, doi:10.1002/qj.49711649103.
- 791 Neal, R., D. Fereday, R. Crocker, and R. E. Comer, 2016: A flexible approach to defining weather  
792 patterns and their application in weather forecasting over europe. *Meteorological Applications*,  
793 **23 (3)**, 389–400, doi:10.1002/met.1563.
- 794 Norwood, A., E. Kalnay, K. Ide, S.-C. Yang, and C. Wolfe, 2013: Lyapunov, singular and bred  
795 vectors in a multi-scale system: an empirical exploration of vectors related to instabilities.  
796 *Journal of Physics A: Mathematical and Theoretical*, **46 (25)**, 254 021, doi:10.1088/1751-8113/  
797 46/25/254021.

- 798 O’Kane, T. J., R. J. Matear, M. A. Chamberlain, J. S. Risbey, B. M. Sloyan, and I. Horenko, 2013a:  
799 Decadal variability in an ogcm southern ocean: Intrinsic modes, forced modes and metastable  
800 states. *Ocean Modelling*, **69**, 1–21, doi:10.1016/j.ocemod.2013.04.009.
- 801 O’Kane, T. J., D. P. Monselesan, J. S. Risbey, I. Horenko, and C. L. E. Franzke, 2017: On memory,  
802 dimension, and atmospheric teleconnections. *Mathematics of Climate and Weather Forecasting*,  
803 **3**, 1–27, doi:10.1515/mcwf-2017-0001.
- 804 O’Kane, T. J., J. S. Risbey, C. Franzke, I. Horenko, and D. P. Monselesan, 2013b: Changes in the  
805 metastability of the midlatitude southern hemisphere circulation and the utility of nonstationary  
806 cluster analysis and split-flow blocking indices as diagnostic tools. *Journal of the atmospheric*  
807 *sciences*, **70** (3), 824–842, doi:10.1175/JAS-D-12-028.1.
- 808 O’Kane, T. J., J. S. Risbey, D. P. Monselesan, I. Horenko, and C. L. Franzke, 2016: On the dynamics  
809 of persistent states and their secular trends in the waveguides of the southern hemisphere  
810 troposphere. *Climate Dynamics*, **46** (11-12), 3567–3597, doi:10.1007/s00382-015-2786-8.
- 811 Oseledets, V. I., 1968: A multiplicative ergodic theorem. characteristic l’apunov, exponents of  
812 dynamical systems. *Trudy Moskovskogo Matematicheskogo Obshchestva*, **19**, 179–210.
- 813 Pedregosa, F., and Coauthors, 2011: Scikit-learn: Machine learning in Python. *Journal of Machine*  
814 *Learning Research*, **12**, 2825–2830.
- 815 Plaut, G., and E. Simmonet, 2001: Large-scale circulation classification, weather regimes, and  
816 local climate over France, the Alps and Western Europe. *Climate Research*, **17**, 303 – 324,  
817 doi:10.3354/cr017303.
- 818 Pohl, B., and N. Fauchereau, 2012: The Southern Annular Mode Seen through Weather Regimes.  
819 *Journal of Climate*, **25** (9), 3336–3354, doi:10.1175/JCLI-D-11-00160.1.



- 820 Quinn, C., T. J. O’Kane, and V. Kitsios, 2020: Application of a local attractor dimension to reduced  
821 space strongly coupled data assimilation for chaotic multiscale systems. *Nonlinear Processes in*  
822 *Geophysics*, **27** (1), 51–74, doi:10.5194/npg-27-51-2020.
- 823 Renwick, J. A., 2005: Persistent Positive Anomalies in the Southern Hemisphere Circulation.  
824 *Monthly Weather Review*, **133** (4), 977–988, doi:10.1175/MWR2900.1.
- 825 Risbey, J. S., T. J. O’Kane, D. P. Monselesan, C. L. E. Franzke, and I. Horenko, 2018: On the  
826 dynamics of austral heat waves. *Journal of Geophysical Research: Atmospheres*, **123** (1), 38–57,  
827 doi:10.1002/2017JD027222.
- 828 Risbey, J. S., T. J. O’Kane, D. P. Monselesan, C. Franzke, and I. Horenko, 2015: Metastability of  
829 northern hemisphere teleconnection modes. *Journal of the Atmospheric Sciences*, **72** (1), 35–54,  
830 doi:10.1175/JAS-D-14-0020.1.
- 831 Ruelle, D., 1979: Ergodic theory of differentiable dynamical systems. *Publications Mathématiques*  
832 *de l’Institut des Hautes Études Scientifiques*, **50** (1), 27–58, doi:10.1007/BF02684768.
- 833 Schubert, S., and V. Lucarini, 2015: Covariant lyapunov vectors of a quasi-geostrophic baroclinic  
834 model: analysis of instabilities and feedbacks. *Quarterly Journal of the Royal Meteorological*  
835 *Society*, **141** (693), 3040–3055, doi:10.1002/qj.2588.
- 836 Schubert, S., and V. Lucarini, 2016: Dynamical analysis of blocking events: spatial and tempo-  
837 ral fluctuations of covariant lyapunov vectors. *Quarterly Journal of the Royal Meteorological*  
838 *Society*, **142** (698), 2143–2158, doi:10.1002/qj.2808.
- 839 Shabbar, A., J. Huang, and K. Higuchi, 2001: The relationship between the wintertime north atlantic  
840 oscillation and blocking episodes in the north atlantic. *International Journal of Climatology*,  
841 **21** (3), 355–369, doi:10.1002/joc.612.

- 842 Sharafi, N., M. Timme, and S. Hallerberg, 2017: Critical transitions and perturbation growth  
843 directions. *Physical Review E*, **96** (3), 032 220, doi:10.1103/PhysRevE.96.032220.
- 844 Smyth, P., K. Ide, and M. Ghil, 1999: Multiple Regimes in Northern Hemisphere Height Fields  
845 via MixtureModel Clustering\*. *Journal of the Atmospheric Sciences*, **56** (21), 3704–3723, doi:  
846 10.1175/1520-0469(1999)056<3704:MRINHH>2.0.CO;2.
- 847 Stan, C., and D. M. Straus, 2007: Is Blocking a Circulation Regime? *Monthly Weather Review*,  
848 **135** (6), 2406–2413, doi:10.1175/MWR3410.1.
- 849 Stephenson, D. B., V. Pavan, and R. Bojariu, 2000: Is the north atlantic oscillation a random walk?  
850 *International Journal of Climatology: A Journal of the Royal Meteorological Society*, **20** (1),  
851 1–18, doi:10.1002/(SICI)1097-0088(200001)20:1%3C1::AID-JOC456%3E3.0.CO;2-P.
- 852 Stone, R. C., 1989: Weather types at brisbane, queensland: an example of the use of principal  
853 components and cluster analysis. *International Journal of Climatology*, **9** (1), 3–32, doi:10.  
854 1002/joc.3370090103.
- 855 Straus, D. M., S. Corti, and F. Molteni, 2007: Circulation Regimes: Chaotic Variability versus  
856 SST-Forced Predictability. *Journal of Climate*, **20** (10), 2251–2272, doi:10.1175/JCLI4070.1.
- 857 Straus, D. M., F. Molteni, and S. Corti, 2017: Atmospheric regimes: The link between weather and  
858 the large-scale circulation. *Nonlinear and Stochastic Climate Dynamics*, C. L. E. Franzke, and  
859 T. J. O’Kane, Eds., Cambridge University Press, chap. 4, 105–135, doi:10.1017/9781316339251.  
860 005.
- 861 Tantet, A., F. R. van der Burgt, and H. A. Dijkstra, 2015: An early warning indicator for atmospheric  
862 blocking events using transfer operators. *Chaos: An Interdisciplinary Journal of Nonlinear  
863 Science*, **25** (3), 036 406, doi:10.1063/1.4908174.

- 864 Trevisan, A., and F. Pancotti, 1998: Periodic orbits, lyapunov vectors, and singular vec-  
865 tors in the lorenz system. *Journal of the atmospheric sciences*, **55** (3), 390–398, doi:  
866 10.1175/1520-0469(1998)055%3C0390:POLVAS%3E2.0.CO;2.
- 867 Vallis, G. K., E. P. Gerber, P. J. Kushner, and B. A. Cash, 2004: A Mechanism and Simple Dynam-  
868 ical Model of the North Atlantic Oscillation and Annular Modes. *Journal of the Atmospheric*  
869 *Sciences*, **61** (3), 264–280, doi:10.1175/1520-0469(2004)061<0264:AMASDM>2.0.CO;2.
- 870 Vautard, R., 1990: Multiple Weather Regimes over the North Atlantic: Analysis of Precursors  
871 and Successors. *Monthly Weather Review*, **118** (10), 2056–2081, doi:10.1175/1520-0493(1990)  
872 118<2056:MWROTN>2.0.CO;2.
- 873 Vercauteren, N., and R. Klein, 2015: A Clustering Method to Characterize Intermittent Bursts of  
874 Turbulence and Interaction with Submesosotions in the Stable Boundary Layer. *Journal of the*  
875 *Atmospheric Sciences*, **72** (4), 1504–1517, doi:10.1175/JAS-D-14-0115.1.
- 876 Vercauteren, N., L. Mahrt, and R. Klein, 2016: Investigation of interactions between scales of  
877 motion in the stable boundary layer. *Quarterly Journal of the Royal Meteorological Society*,  
878 **142** (699), 2424–2433, doi:10.1002/qj.2835.
- 879 Visbeck, M. H., J. W. Hurrell, L. Polvani, and H. M. Cullen, 2001: The north atlantic oscillation:  
880 past, present, and future. *Proceedings of the National Academy of Sciences*, **98** (23), 12 876–  
881 12 877, doi:10.1073/pnas.231391598.
- 882 Wolfe, C. L., and R. M. Samelson, 2007: An efficient method for recovering lyapunov vectors  
883 from singular vectors. *Tellus A: Dynamic Meteorology and Oceanography*, **59** (3), 355–366,  
884 doi:10.1111/j.1600-0870.2007.00234.x.

885 Woollings, T., B. Hoskins, M. Blackburn, and P. Berrisford, 2008: A new rossby wave–breaking  
886 interpretation of the north atlantic oscillation. *Journal of the Atmospheric Sciences*, **65** (2),  
887 609–626, doi:10.1175/2007JAS2347.1.

888 **LIST OF TABLES**

889 **Table 1.** Summary statistics for the run lengths (in days) of consecutive days assigned to  
 890 each state for the model with  $K = 3$ ,  $m = 3$  days, and  $p = 5$  days. . . . . 46

891 **Table 2.** Counts of number of transitions and the total number of days assigned to each  
 892 state, stratified by season. Transitions are assigned to the season corresponding  
 893 to the last day in the initial state. Note that  $m_{\max} = 5$  days are held out as  
 894 presample values from the full record of  $T = 14610$  days, yielding a total fit  
 895 period of 14605 days. . . . . 47

896 **Table 3.** Probabilities associated with the occurrence of positive FTCLEs for short and  
 897 long push forward steps. Note that the total number of days for which the CLVs  
 898 are calculated depends on the push forward step ( $T_M = 14605 - 2M$  days). . . . . 48

899 **Table 4.** Average  $\dim_{KY}(t)$  measure by state. The first column is averaged over all days  
 900 associated with each state. The second column averages over the associated  
 901 days using a 5-day filter, namely only taking the values from time instances  
 902 where the 2 days before and the 2 days after are also associated with the same  
 903 state. . . . . 49

904 **Table 5.** Characteristics of unstable patterns associated with transitions to and from  
 905 persistent states (shown in FIG. 6). The day column refers to the day in the end  
 906 state after the transition. . . . . 50

907 TABLE 1. Summary statistics for the run lengths (in days) of consecutive days assigned to each state for the  
 908 model with  $K = 3$ ,  $m = 3$  days, and  $p = 5$  days.

		DJF	MAM	JJA	SON	ALL
AR	Min.	1	1	1	1	1
	Mean	2.8	2.4	2.5	2.9	2.7
	Max.	21	13	15	18	21
NAO <sup>-</sup>	Min.	1	1	1	1	1
	Mean	2.5	4.3	9.3	3.2	4.7
	Max.	21	38	63	29	63
NAO <sup>+</sup>	Min.	1	1	1	1	1
	Mean	3.3	2.4	2.2	2.4	2.7
	Max.	26	11	10	12	26

909 TABLE 2. Counts of number of transitions and the total number of days assigned to each state, stratified by  
 910 season. Transitions are assigned to the season corresponding to the last day in the initial state. Note that  $m_{\max} = 5$   
 911 days are held out as presample values from the full record of  $T = 14610$  days, yielding a total fit period of 14605  
 912 days.

		DJF	MAM	JJA	SON	ALL
Transitions	AR to NAO <sup>-</sup>	136	213	168	234	751
	AR to NAO <sup>+</sup>	310	147	44	209	710
	NAO <sup>-</sup> to AR	118	197	176	219	710
	NAO <sup>-</sup> to NAO <sup>+</sup>	177	214	131	228	750
	NAO <sup>+</sup> to AR	327	153	42	228	750
	NAO <sup>+</sup> to NAO <sup>-</sup>	163	218	129	200	710
Any		1232	1142	690	1318	4381
Days assigned to	AR	1229	859	539	1274	3901
	NAO <sup>-</sup>	725	1974	2771	1326	6796
	NAO <sup>+</sup>	1651	847	370	1040	3908
	Any	3605	3680	3680	3640	14605

913 TABLE 3. Probabilities associated with the occurrence of positive FTCLEs for short and long push forward  
 914 steps. Note that the total number of days for which the CLVs are calculated depends on the push forward step  
 915 ( $T_M = 14605 - 2M$  days).

		$M = 3$	$M = 10$	$M = 30$	$M = 50$
$P(\dim_{KY} > 0)$	AR	0.392	0.004	0.002	0.003
	NAO <sup>-</sup>	0.992	0.002	0.001	0
	NAO <sup>+</sup>	0.624	0.007	0.001	0.001
	Any	0.733	0.004	0.001	0.001



916 TABLE 4. Average  $\dim_{KY}(t)$  measure by state. The first column is averaged over all days associated with each  
917 state. The second column averages over the associated days using a 5-day filter, namely only taking the values  
918 from time instances where the 2 days before and the 2 days after are also associated with the same state.

	no filter	5-day filter
AR	0.84	0
NAO <sup>-</sup>	2.55	2.98
NAO <sup>+</sup>	1.16	1.28

919 TABLE 5. Characteristics of unstable patterns associated with transitions to and from persistent states (shown  
 920 in FIG. 6). The day column refers to the day in the end state after the transition.

Pattern	Transition	day	CLV	FTCLE
	NAO <sup>-</sup> to AR	1	1	0.029
A	NAO <sup>-</sup> to NAO <sup>+</sup>	1	1	0.058
	NAO <sup>-</sup> to NAO <sup>+</sup>	2	2	0.012
B	NAO <sup>-</sup> to NAO <sup>+</sup>	1	2	0.023
C	NAO <sup>+</sup> to AR	2	2	0.017
	NAO <sup>-</sup> to NAO <sup>+</sup>	2	1	0.031
D	NAO <sup>+</sup> to NAO <sup>-</sup>	1	1	0.027

921 **LIST OF FIGURES**

922 **Fig. 1.** Mean test set reconstruction error as a function of typical state length  $p$  (main figure), and  
923 zoom to the region containing the model with minimal mean reconstruction RMSE (inset).  
924 Note that  $p = 0$  corresponds to no persistence constraint imposed (i.e.,  $C_T \rightarrow \infty$ ). Error bars  
925 show the approximate one standard error ranges, and for clarity models with the same VAR  
926 order  $m$  are offset in the  $x$ -direction. The minimal mean reconstruction RMSE occurs for  
927  $K = 3$ ,  $m = 3$  days, and  $p = 5$  days. . . . . 53

928 **Fig. 2.** Composites of  $Z'_{g500hPa}$  in each of the FEM-BV-VAR states for the model with  $K = 3$ ,  $m = 3$   
929 days, and  $p = 5$  days. Shading indicates regions for which the composite value lies outside  
930 of the interval containing  $100(1 - \alpha) = 99\%$  of 1000 bootstrap samples drawn assuming the  
931 number of samples assigned to each state is fixed. . . . . 54

932 **Fig. 3.** Model NAO<sup>-</sup> state residency percent compared to residency percent for occurrences of a  
933 negative CPC NAO index value using a sliding window of one year (top) and yearly average  
934 with LOWESS smoothing (bottom). . . . . 55

935 **Fig. 4.** Statistics of the finite-time growth rates for the leading 10 CLVs computed using varying  
936 push forward steps ( $M = 3, 10, 30, 50$ ) compared to their asymptotic growth rates. . . . . 56

937 **Fig. 5.** Physical projections of unstable CLVs in persistent states. . . . . 57

938 **Fig. 6.** Physical projections of unstable CLVs at transitions associated with persistent states. . . . . 58

939 **Fig. 7.** Transient behavior of the leading CLV alignments ( $\theta_{1,2}$ ,  $\theta_{2,3}$ , and  $\theta_{1,3}$ ), growth rates ( $\Lambda_1$ ,  $\Lambda_2$ ,  
940 and  $\Lambda_3$ ), and finite-time dimension for two different but representative time segments using  
941 push forward  $M = 3$ . We also plot the state indicators to compare to transitions. . . . . 59

942 **Fig. 8.** Box and whisker plots of  $\theta_{1,2}$ ,  $\theta_{2,3}$ , and  $\theta_{1,3}$  around each transition with Day 0 indicating  
943 the last day in the previous state and Day 1 the first day in the following state. Diamonds  
944 indicate outlier values. The transitions have been filtered to only include those associated  
945 with residencies longer than 4 days both before and after the transition. . . . . 60

946 **Fig. 9.** Collective trajectories of  $\theta_{1,2}$ ,  $\theta_{2,3}$ , and  $\theta_{1,3}$  separated by specific transition. The transitions  
947 have been filtered as in FIG. 8. . . . . 61

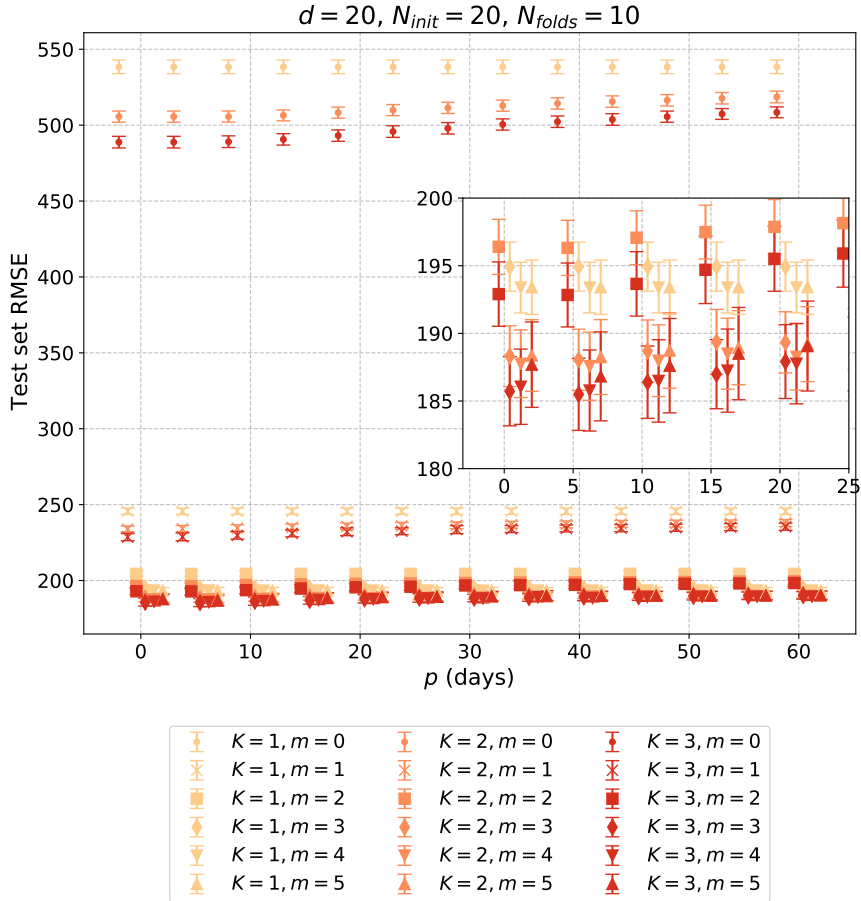
948 **Fig. 10.** (a) Alignment of the leading two CLVs for different push forward steps. From top to  
949 bottom: raw NAO<sup>-</sup> signal,  $M = 3$ ,  $M = 10$ ,  $M = 30$ ,  $M = 50$ . (b) Power spectral density of  
950 the corresponding alignment time series. Red dots (crosses) indicate peaks that are 2 (3)  
951 standard deviations away from neighboring measures. . . . . 62

952 **Fig. 11.** Alignment of the leading two CLVs for push forward step  $M = 50$  compared to transition  
953 index calculated from Eq. (18). . . . . 63

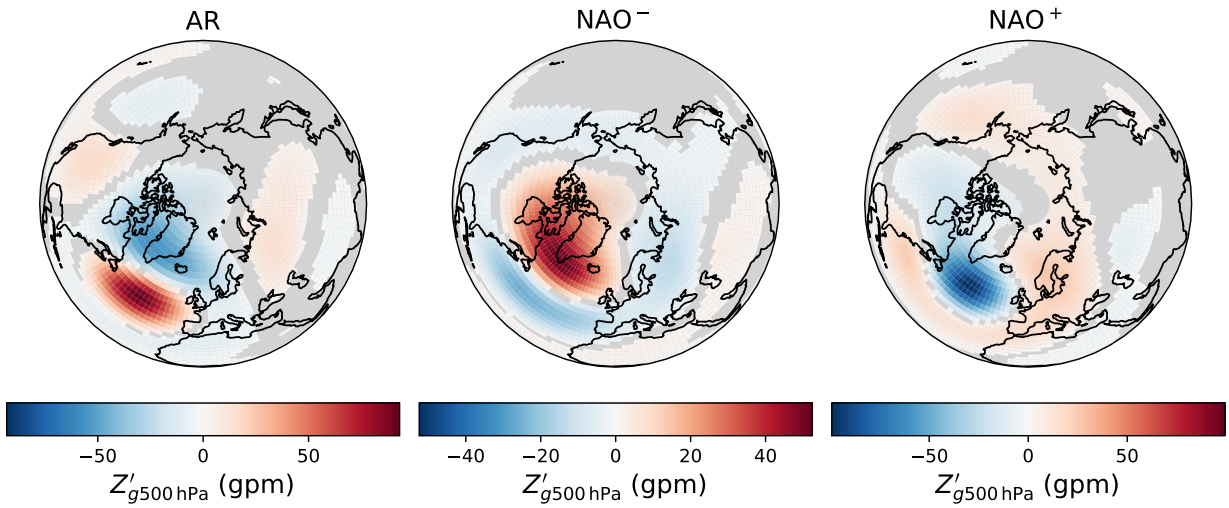
954 **Fig. 12.** Comparison of average alignment ( $\overline{\theta_{i,j}}$ ) of leading CLVs by season for push forward  $M = 50$ .  
955 We see the strong alignment emerging in the JJA  $\theta_{1,2}$ , and a weak alignment in both SON  
956 and DJF. Additionally we observe some seasonality in  $\theta_{2,3}$  and  $\theta_{3,4}$ , with both peaking in DJF. . . . . 64

957 **Fig. A1.** Leading 20 modes of variability in the North Atlantic sector (20°N-90°N and 110°W-0°E)  
958 of the daily NCEP/NCAR reanalysis data (Kalnay et al. 1996). All EOFs use the same color  
959 scale shown at the bottom. . . . . 65

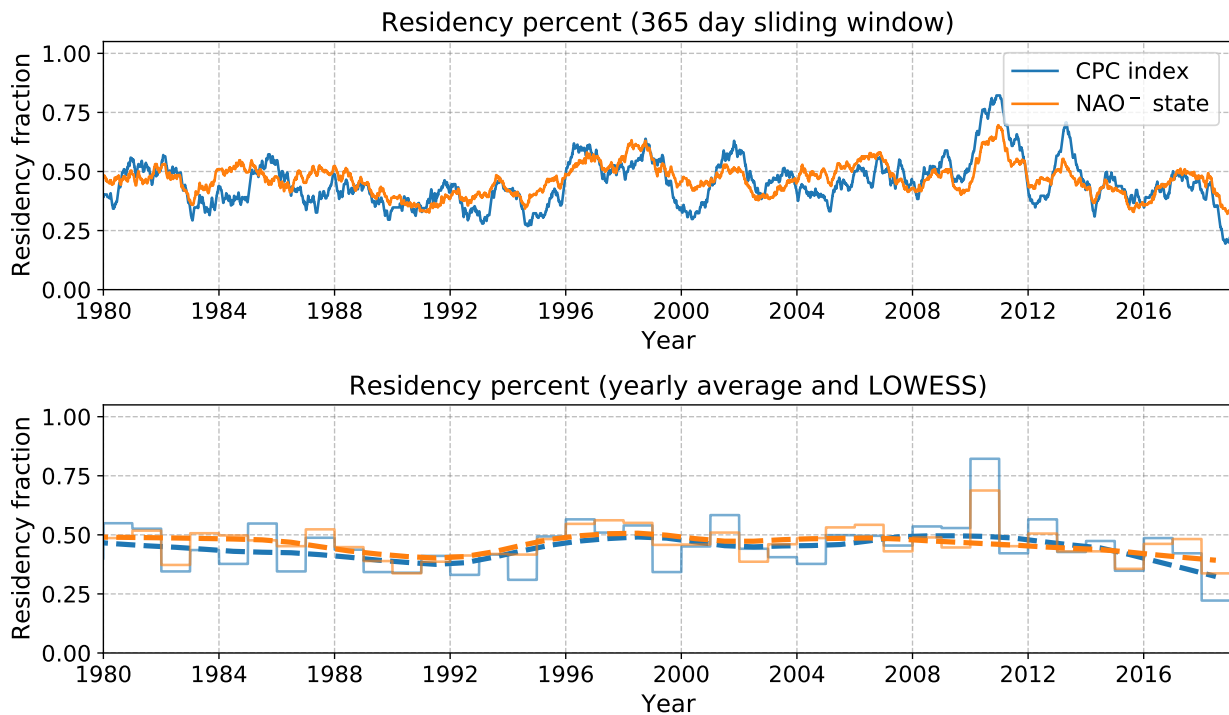
960	<b>Fig. D1.</b> Atlantic Ridge to negative NAO. . . . .	66
961	<b>Fig. D2.</b> Atlantic Ridge to positive NAO. . . . .	67
962	<b>Fig. D3.</b> Negative NAO to Atlantic Ridge. . . . .	68
963	<b>Fig. D4.</b> Negative NAO to positive NAO. . . . .	69
964	<b>Fig. D5.</b> Positive NAO to Atlantic Ridge. . . . .	70
965	<b>Fig. D6.</b> Positive NAO to negative NAO. . . . .	71



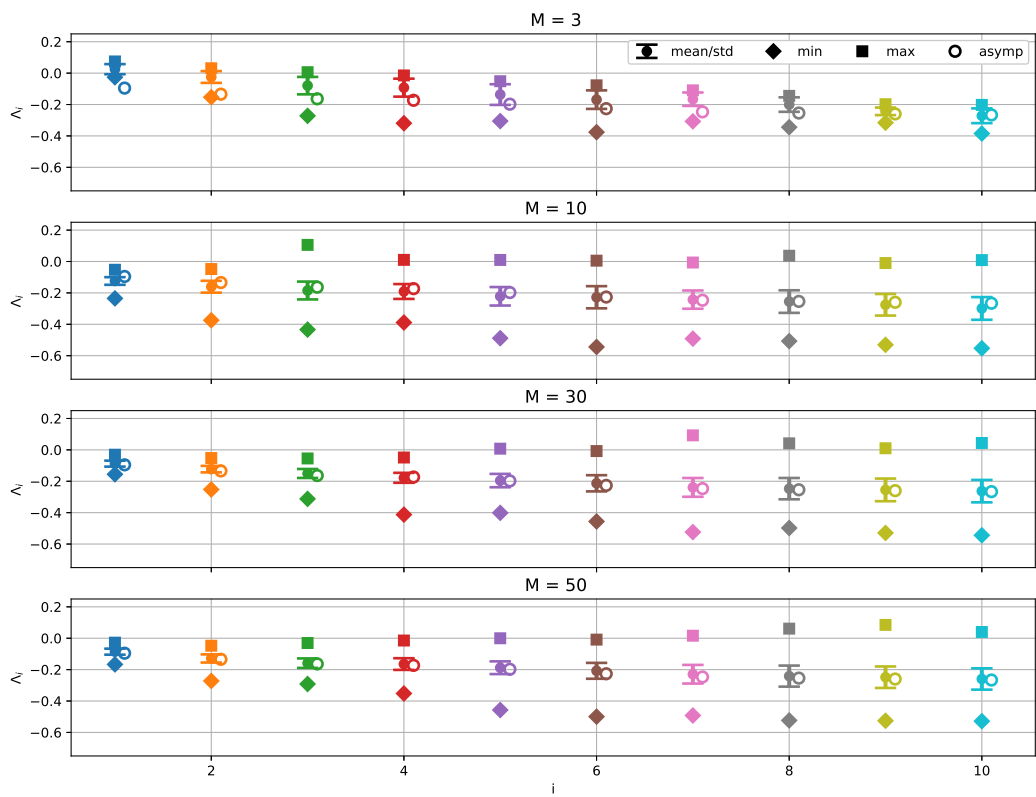
966 FIG. 1. Mean test set reconstruction error as a function of typical state length  $p$  (main figure), and zoom to the  
 967 region containing the model with minimal mean reconstruction RMSE (inset). Note that  $p = 0$  corresponds to no  
 968 persistence constraint imposed (i.e.,  $C_T \rightarrow \infty$ ). Error bars show the approximate one standard error ranges, and  
 969 for clarity models with the same VAR order  $m$  are offset in the  $x$ -direction. The minimal mean reconstruction  
 970 RMSE occurs for  $K = 3, m = 3$  days, and  $p = 5$  days.



971 FIG. 2. Composites of  $Z'_{g500hPa}$  in each of the FEM-BV-VAR states for the model with  $K = 3$ ,  $m = 3$  days,  
 972 and  $p = 5$  days. Shading indicates regions for which the composite value lies outside of the interval containing  
 973  $100(1 - \alpha) = 99\%$  of 1000 bootstrap samples drawn assuming the number of samples assigned to each state is  
 974 fixed.



975 FIG. 3. Model  $NAO^-$  state residency percent compared to residency percent for occurrences of a negative  
 976 CPC NAO index value using a sliding window of one year (top) and yearly average with LOWESS smoothing  
 977 (bottom).



978 FIG. 4. Statistics of the finite-time growth rates for the leading 10 CLVs computed using varying push forward  
 979 steps ( $M = 3, 10, 30, 50$ ) compared to their asymptotic growth rates.



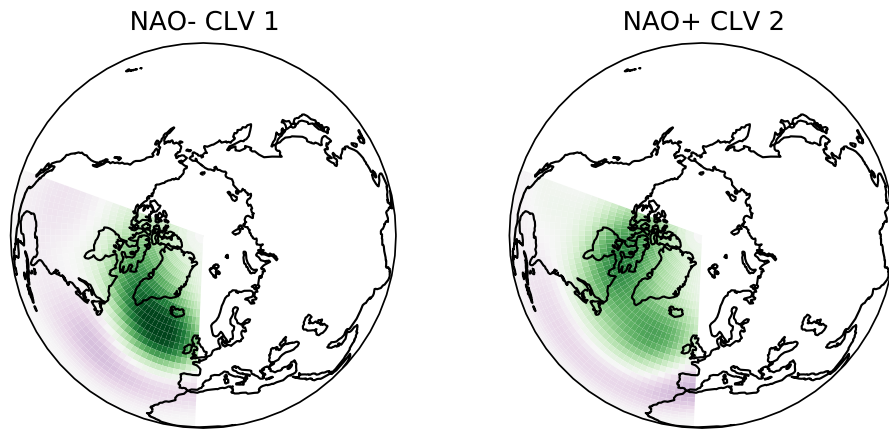


FIG. 5. Physical projections of unstable CLVs in persistent states.

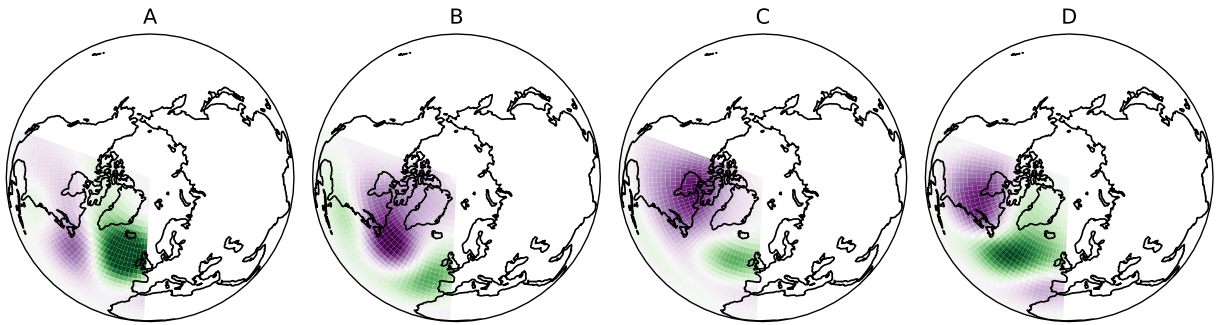
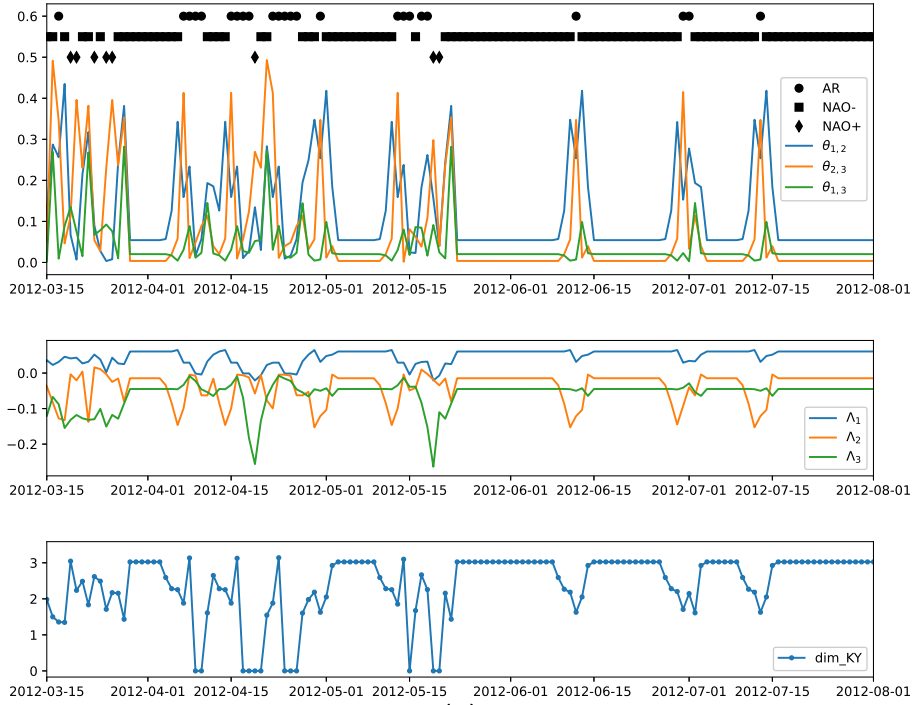
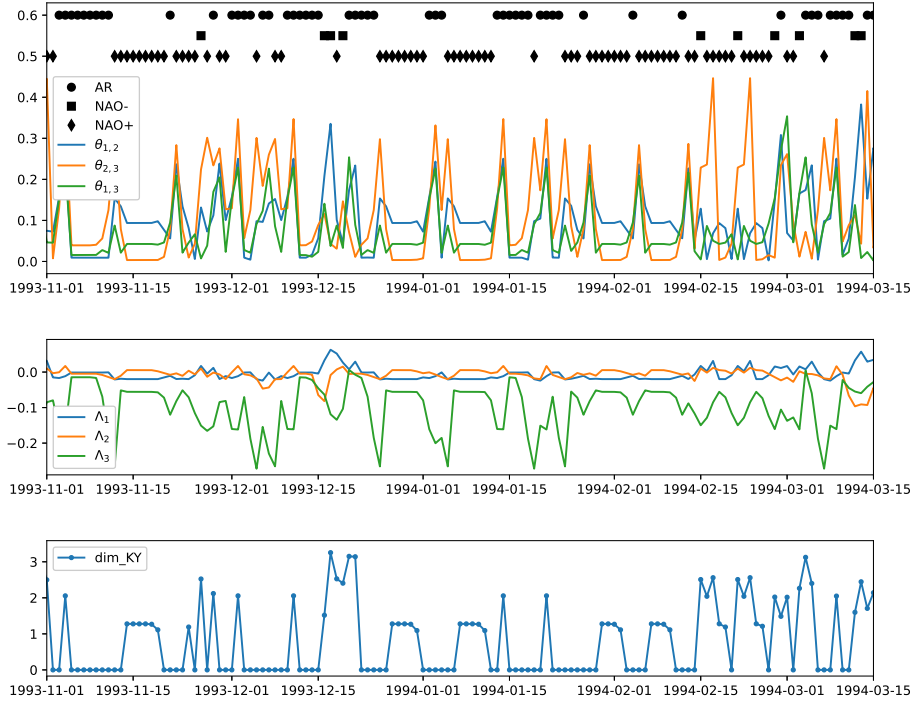


FIG. 6. Physical projections of unstable CLVs at transitions associated with persistent states.

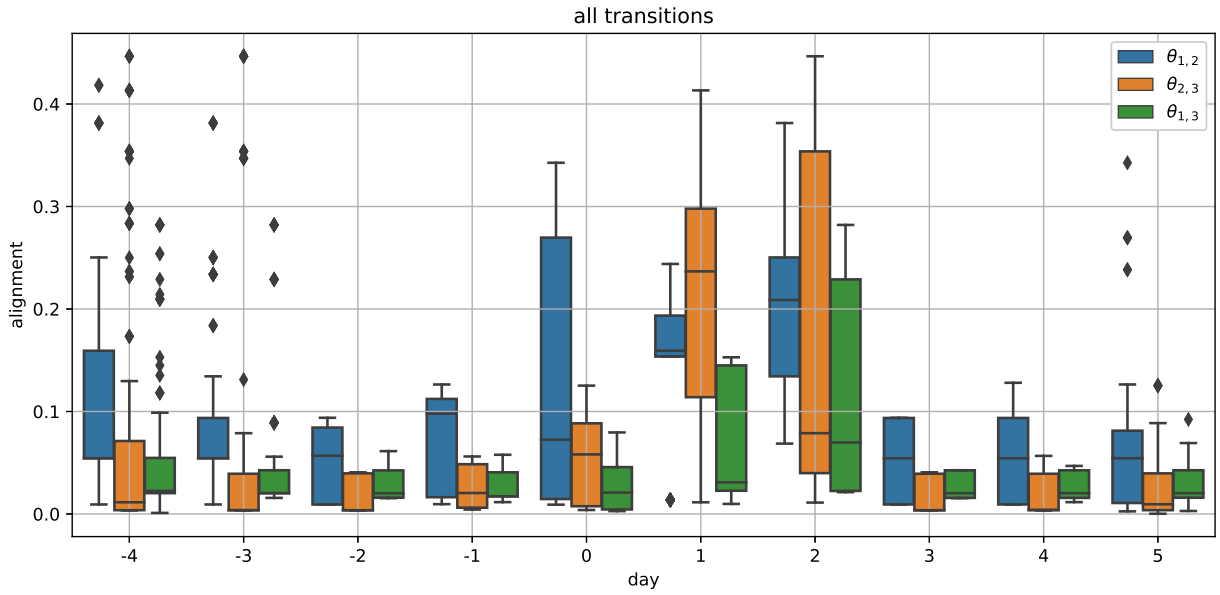


(a)

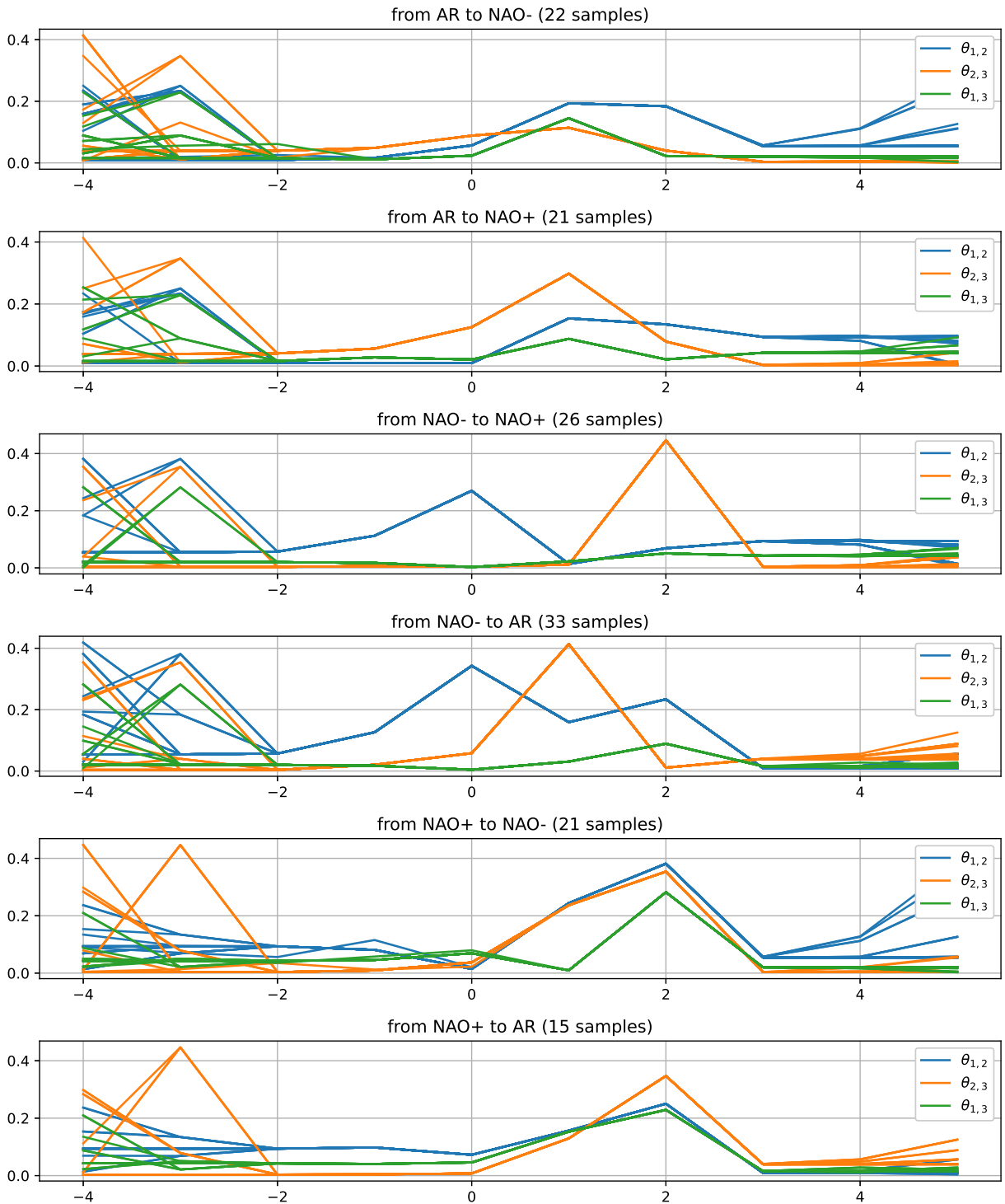


(b)

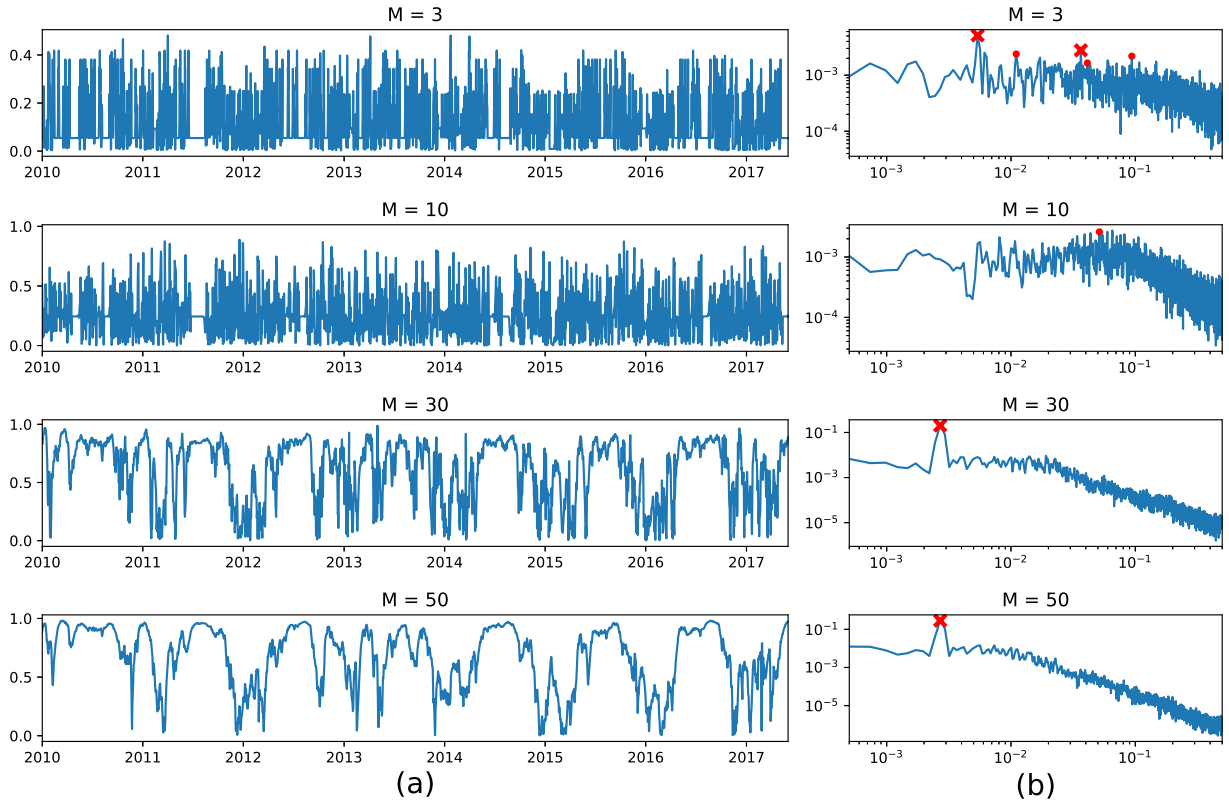
980 FIG. 7. Transient behavior of the leading CLV alignments ( $\theta_{1,2}$ ,  $\theta_{2,3}$ , and  $\theta_{1,3}$ ), growth rates ( $\Lambda_1$ ,  $\Lambda_2$ , and  $\Lambda_3$ ),  
 981 and finite-time dimension for two different but representative time segments using push forward  $M = 3$ . We also  
 982 plot the state indicators to compare to transitions.



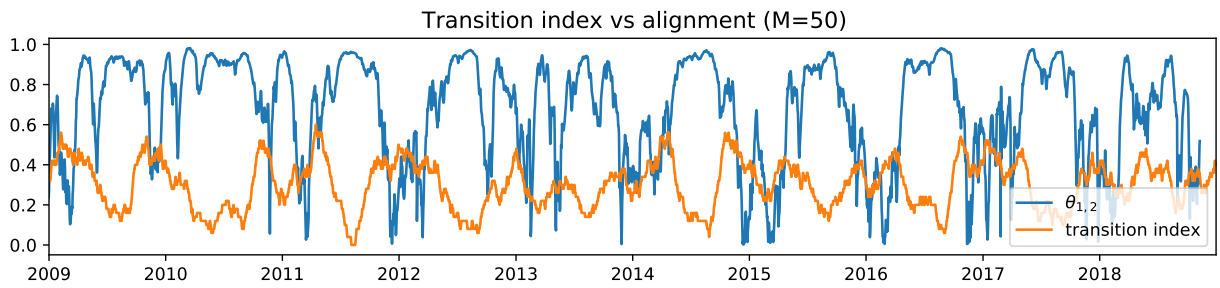
983 FIG. 8. Box and whisker plots of  $\theta_{1,2}$ ,  $\theta_{2,3}$ , and  $\theta_{1,3}$  around each transition with Day 0 indicating the last day in  
 984 the previous state and Day 1 the first day in the following state. Diamonds indicate outlier values. The transitions  
 985 have been filtered to only include those associated with residencies longer than 4 days both before and after the  
 986 transition.



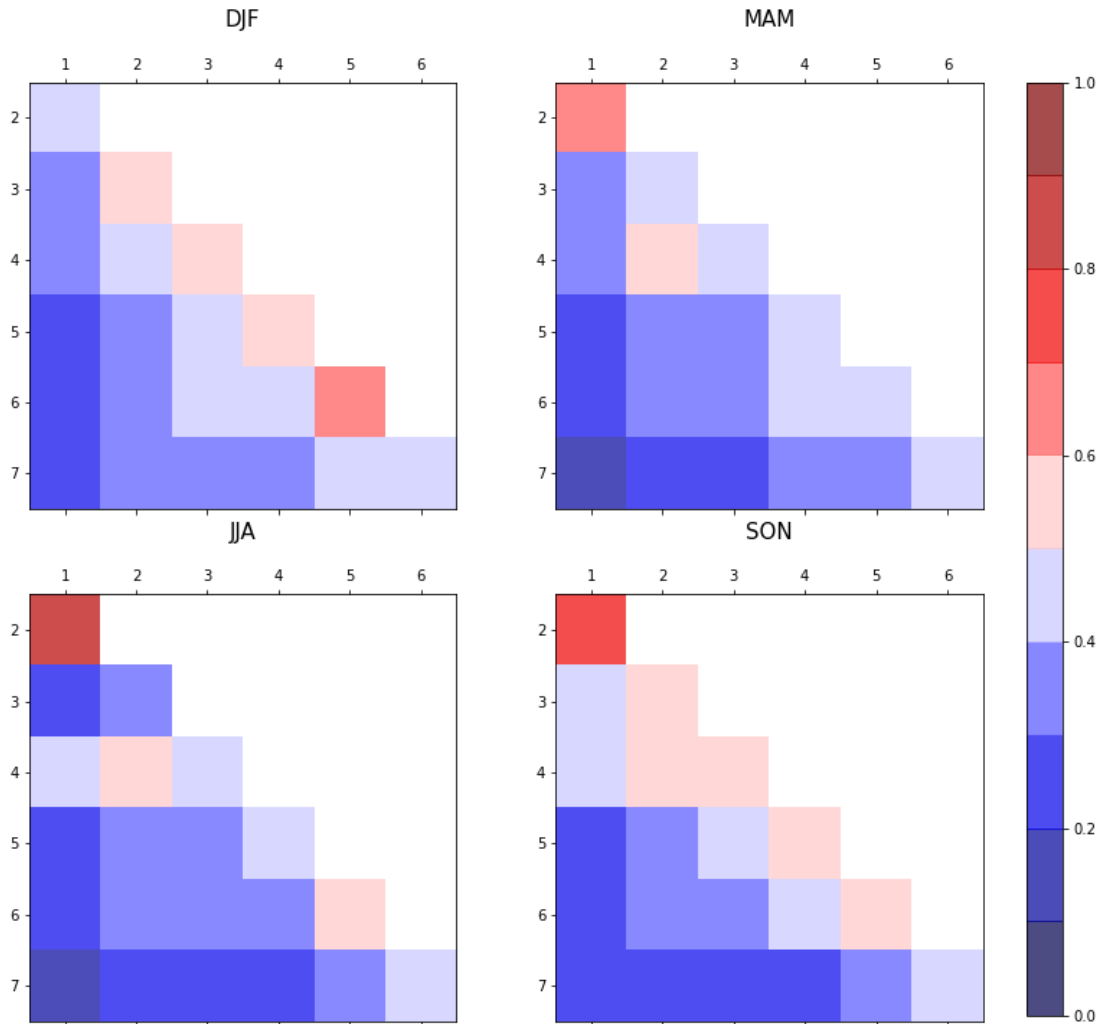
987 FIG. 9. Collective trajectories of  $\theta_{1,2}$ ,  $\theta_{2,3}$ , and  $\theta_{1,3}$  separated by specific transition. The transitions have been  
 988 filtered as in FIG. 8.



989 FIG. 10. (a) Alignment of the leading two CLVs for different push forward steps. From top to bottom: raw  
 990 NAO<sup>-</sup> signal,  $M = 3$ ,  $M = 10$ ,  $M = 30$ ,  $M = 50$ . (b) Power spectral density of the corresponding alignment time  
 991 series. Red dots (crosses) indicate peaks that are 2 (3) standard deviations away from neighboring measures.

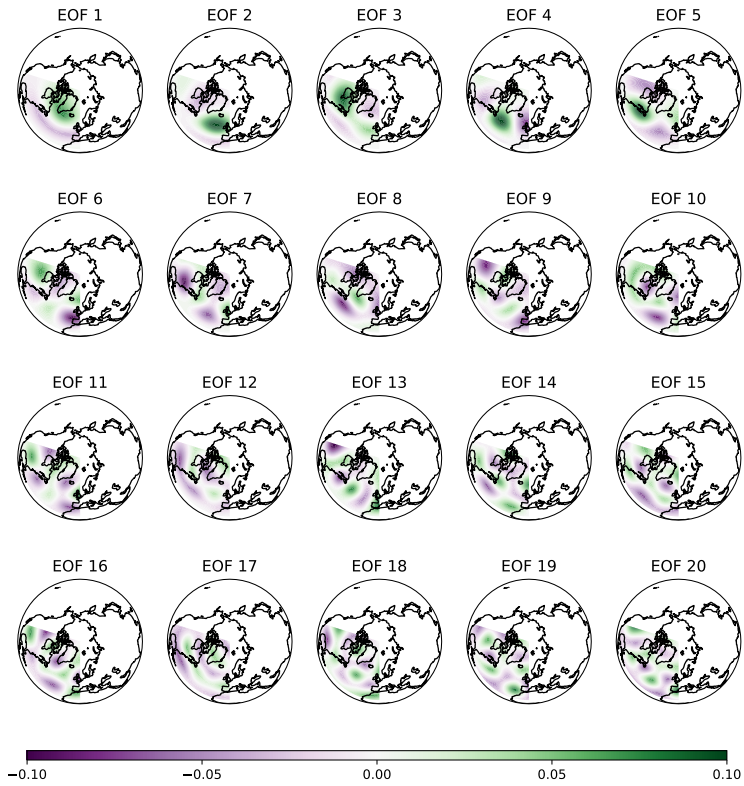


992 FIG. 11. Alignment of the leading two CLVs for push forward step  $M = 50$  compared to transition index  
 993 calculated from Eq. (18).



994 FIG. 12. Comparison of average alignment ( $\overline{\theta_{i,j}}$ ) of leading CLVs by season for push forward  $M = 50$ . We  
 995 see the strong alignment emerging in the JJA  $\overline{\theta_{1,2}}$ , and a weak alignment in both SON and DJF. Additionally we  
 996 observe some seasonality in  $\overline{\theta_{2,3}}$  and  $\overline{\theta_{3,4}}$ , with both peaking in DJF.





997 Fig. A1. Leading 20 modes of variability in the North Atlantic sector (20°N-90°N and 110°W-0°E) of the  
 998 daily NCEP/NCAR reanalysis data (Kalnay et al. 1996). All EOFs use the same color scale shown at the bottom.

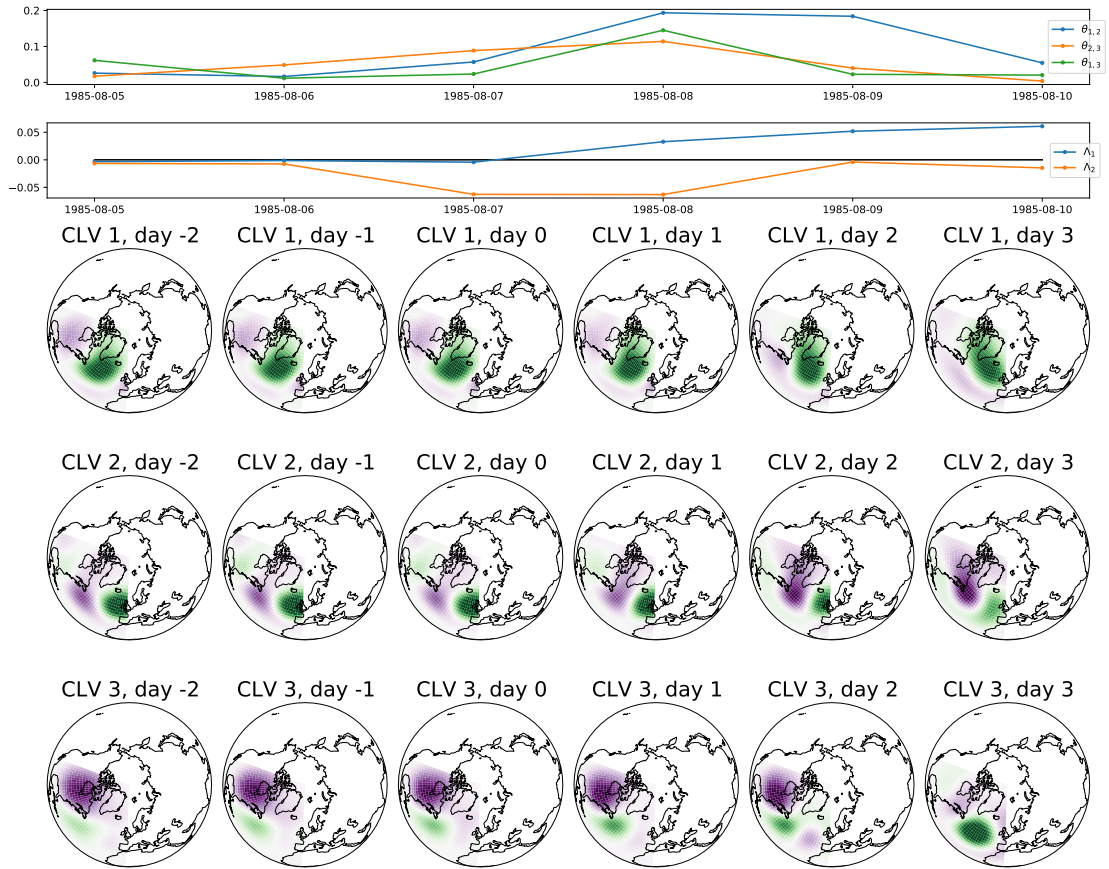


Fig. D1. Atlantic Ridge to negative NAO.

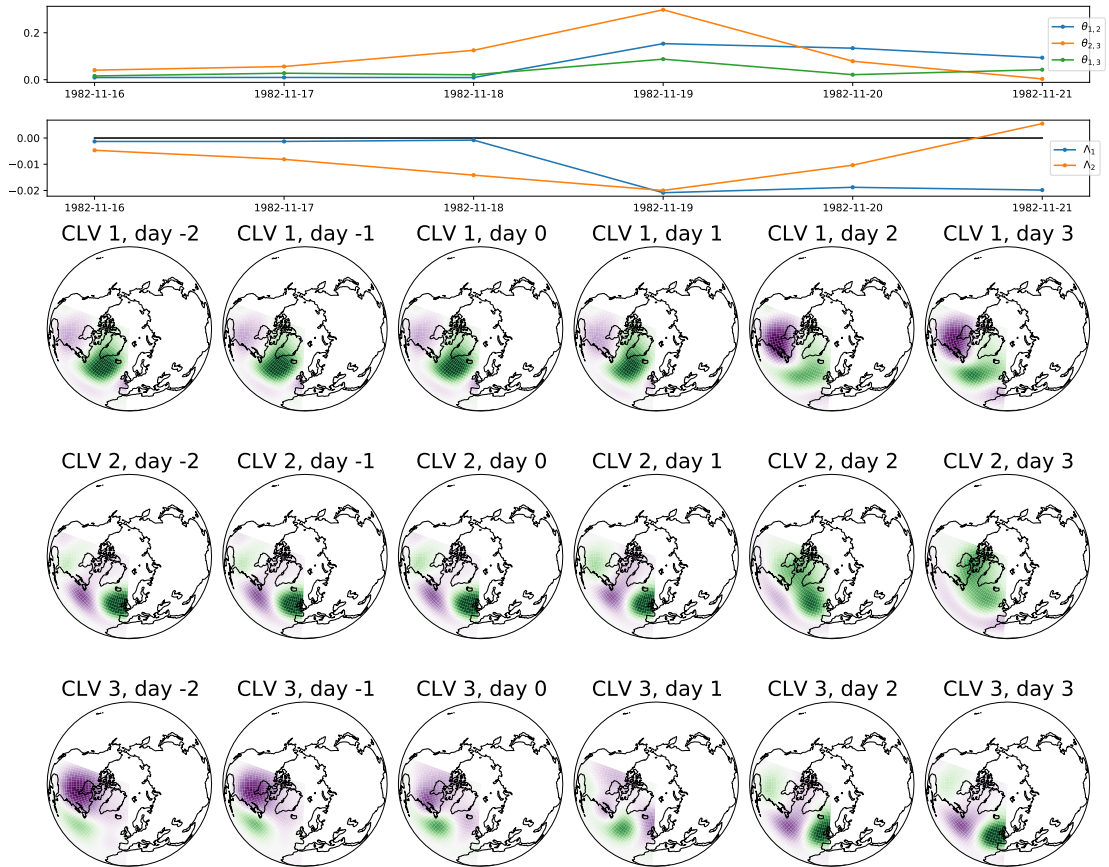


Fig. D2. Atlantic Ridge to positive NAO.

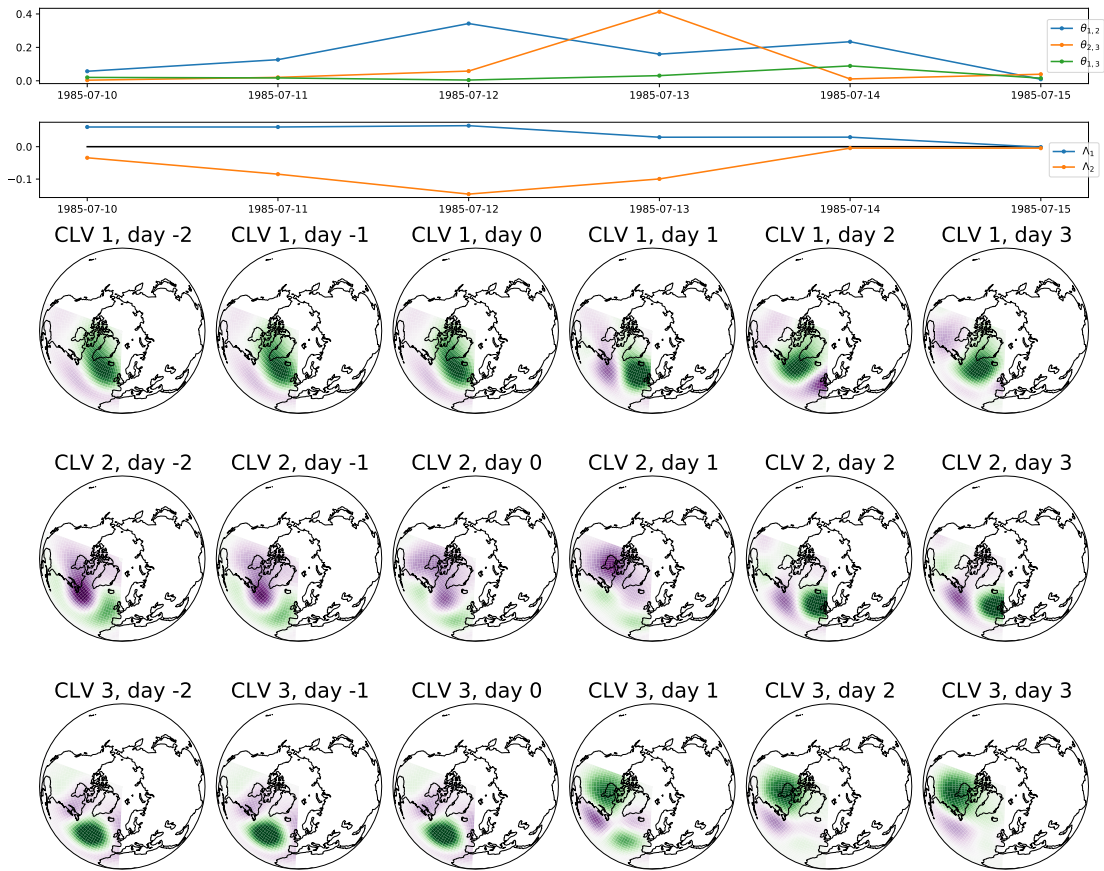


Fig. D3. Negative NAO to Atlantic Ridge.

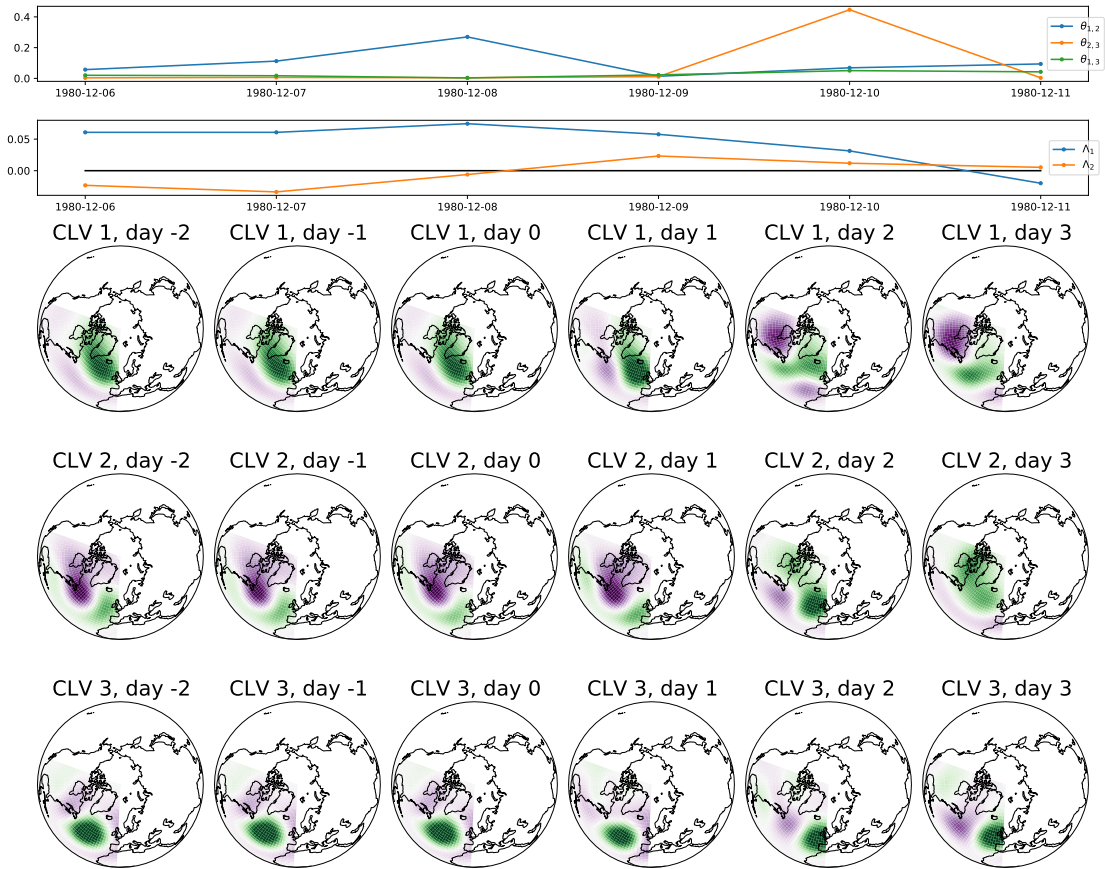


Fig. D4. Negative NAO to positive NAO.

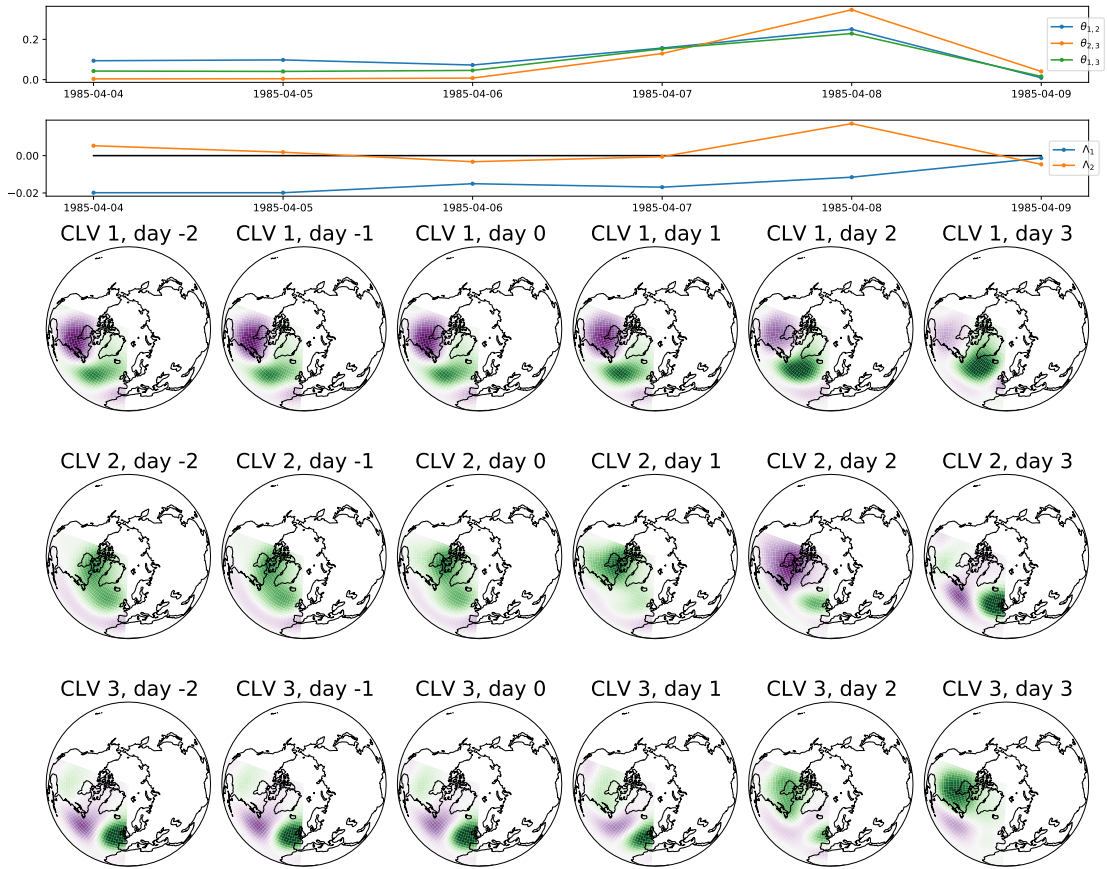


Fig. D5. Positive NAO to Atlantic Ridge.

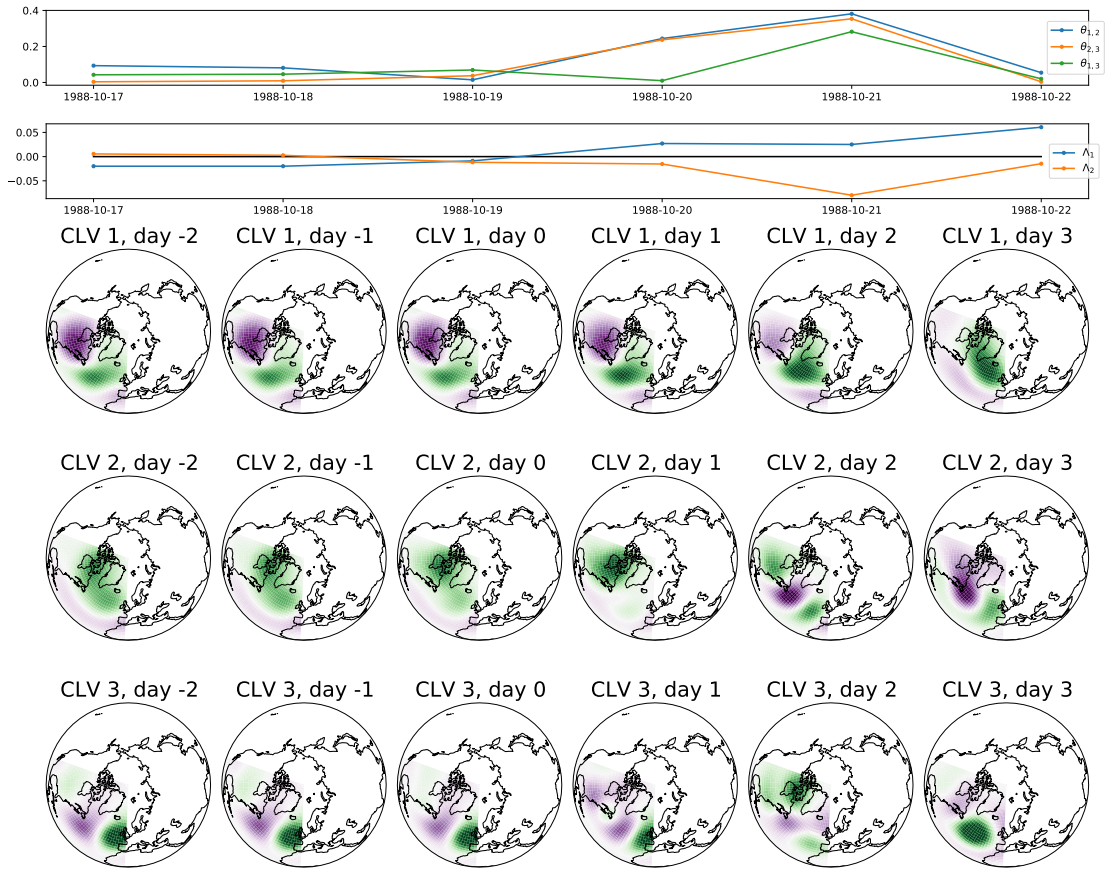


Fig. D6. Positive NAO to negative NAO.